


AUTHOR QUERY FORM

| | | |
|--|-----------------------------|--|
|  ELSEVIER | Journal: YJCPH | Please e-mail your responses and any corrections to: E-mail: corrections.esch@elsevier.vtex.lt |
| | Article Number: 8511 | |

Dear Author,

Please check your proof carefully and mark all corrections at the appropriate place in the proof. **It is crucial that you NOT make direct edits to the PDF using the editing tools as doing so could lead us to overlook your desired changes.** Rather, please request corrections by using the tools in the Comment pane to annotate the PDF and call out the changes you would like to see. To ensure fast publication of your paper please return your corrections within 48 hours.

For correction or revision of any artwork, please consult <http://www.elsevier.com/artworkinstructions>

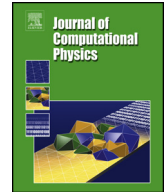
Any queries or remarks that have arisen during the processing of your manuscript are listed below and highlighted by flags in the proof.

| Location in article | Query / Remark: Click on the Q link to find the query's location in text Please insert your reply or correction at the corresponding line in the proof |
|----------------------------|--|
| Q1 | Your article is registered as a regular item and is being processed for inclusion in a regular issue of the journal. If this is NOT correct and your article belongs to a Special Issue/Collection please contact <a.kurian@elsevier.com> immediately prior to returning your corrections. (p. 1/ line 1) |
| Q2 | The author names have been tagged as given names and surnames (surnames are highlighted in teal color). Please confirm if they have been identified correctly and are presented in the desired order. (p. 1/ line 15) |
| Q3 | Figure(s) will appear in black and white in print and in color on the web. The figure(s) contains references to color or the colors are mentioned in the main text. Based on this, the explanatory text about the interpretation of the colors has been added. Please check, and correct if necessary. (p. 4/ line 14) |
| Q4 | Figures 18 and 19 were not cited in the text. Please check that the citations suggested by the copyeditor are in the appropriate place, and correct if necessary. (p. 18/ line 51) |
| Q5 | Ref. [22] has been updated (vol. no, year of publication, pagination). Please check. (p. 25/ line 27) |
| Q6 | Please check and update/or correct the caption of supplementary material. (p. 27/ line 9) |
| Q7 | Please check if sponsor name has been identified correctly and correct if necessary. (p. 28/ line 4) |

| Location in article | Query / Remark: Click on the Q link to find the query's location in text Please insert your reply or correction at the corresponding line in the proof |
|--------------------------------|--|
| | <div data-bbox="569 143 1110 266" style="border: 1px solid black; padding: 5px; width: fit-content; margin: auto;"><p data-bbox="590 157 961 252">Please check this box or indicate your approval if you have no corrections to make to the PDF file</p><input data-bbox="1010 171 1087 233" type="checkbox"/></div> |

Contents lists available at ScienceDirect

Journal of Computational Physics

www.elsevier.com/locate/jcp

A face-smoothed cell method for static and dynamic piezoelectric coupled problems on polyhedral meshes

Federico Moro^{a,*}, Daniele Desideri^a, Alberto Doria^a, Alvisé Maschio^a,
 Cristian Medé^a, Lorenzo Codecasa^b

^a Dipartimento di Ingegneria Industriale, Università degli Studi di Padova, Italy

^b Dipartimento di Elettronica, Informazione e Bioingegneria, Politecnico di Milano, Italy

ARTICLE INFO

Article history:

Received 21 June 2018

Received in revised form 31 December 2018

Accepted 2 February 2019

Available online xxxx

Keywords:

Smoothing

Cell Method

FEM

MEMS

Polyhedral mesh

Piezoelectric

ABSTRACT

Low-order discretization schemes are suitable for modeling 3-D multiphysics problems since a huge number of degrees of freedom (DoFs) is typically required by standard high-order Finite Element Method (FEM). On the other hand, polyhedral meshes ensure a great flexibility in the domain discretization and are thus suitable for complex model geometries. These features are useful for the multiphysics simulation of micro piezoelectric devices with a thin multi-layered and multi-material structure. The Cell Method (CM) is a low-order discretization scheme which has been mainly adopted up to now for electromagnetic problems but has not yet been used for mechanical problems with polyhedral discretization. This work extends the CM to piezo-elasticity by reformulating local constitutive relationships in terms of displacement gradient. In such a way, piecewise uniform edge basis functions defined on arbitrary polyhedral meshes can be used for discretizing local constitutive relationships. With the CM matrix assembly is completely Jacobian-free and do not require Gaussian integration, reducing code complexity. The smoothing technique, firstly introduced for FEM, is here extended to CM in order to avoid shear locking arising when low-order discretization is used for thin cantilevered beams under bending. The smoothed CM is validated for static and dynamic problems on a real test case by comparison with both second-order FEM and experimental data. Numerical results show that accuracy is retained **even a much** lower number of DoFs is required compared to FEM.

© 2019 Elsevier Inc. All rights reserved.

1. Introduction

Piezoelectric materials are nowadays of widespread use for producing actuators, sensors, and energy harvesters for feeding ultra-low power electronics [1]. Analytical models are well assessed and important tools for designing and optimizing piezoelectric devices (piezo-MEMS) [2]. Lumped circuit models are derived for instance in control applications [3]. Non-ideal conditions like clamping setup, local variations in geometry and material properties, and residual stress may significantly affect the device performance, and in particular its resonance frequency. Main issues in the numerical modeling of piezo-MEMS are a large aspect ratio and a multi-layered structure, which requires 3-D electro-mechanical coupled models. First-order finite elements are not suitable to discretize thin structures due to shear and/or volume locking. Therefore,

* Corresponding author.

E-mail address: federico.moro@unipd.it (F. Moro).

<https://doi.org/10.1016/j.jcp.2019.02.012>

0021-9991/© 2019 Elsevier Inc. All rights reserved.

higher-order elements have to be used for accurate analyses even though a large amount of DoFs is required, which limits the model size. Shell and plate elements have thus been proposed in order to overcome such limitations [4]. These models rely on Kirchhoff's or Reissner–Mindlin plate element theories, which provide analytical approximations for displacement field of thin multi-layered structures. Reduced integration or enhanced assumed strains (EAS) are used in order to avoid locking deriving from polynomial approximation.

1.1. Polyhedral methods

Numerical models based on plate theory assumption however are not adequate to predict the behavior of fully 3-D structures (e.g. multilayer structure with a piezoelectric layer embedded within a uniform polymer layer) typical of real-life piezo-MEMS. In this context numerical formulations based on polyhedral meshes (poly-meshes) provide much more flexibility by using arbitrarily shaped elements. For instance, carving out a structured background grid naturally leads to a mesh with polyhedral elements on the boundary. Moreover, the mesh can be locally refined and coarsened much more easily by adopting a poly-mesh (i.e. automatic inclusion of hanging nodes) and standard tetrahedral and hexahedral meshes can be connected very well by using polyhedral transition elements. Different strategies have been proposed in literature for interpolating fields within polyhedrons, e.g. harmonic basis functions [5], natural elements [6], mean value coordinates [7]. However, the construction of shape functions for polyhedral elements is not straightforward as in conventional FEM (e.g., rational functions used as interpolants increase formulation complexity) and very efficient numerical integration techniques are required to limit inaccuracy and computing cost. Moreover, poly-mesh generators are still under development and not yet made available by software producers. These features have strongly limited the adoption of polyhedral finite elements. Recently, Virtual Element Method (VEM) has been proposed in order to avoid an explicit computation of basis functions within polyhedrons. Elementary stiffness matrices are computed from discrete local projection operators, which are defined in turn by solving local matrix systems for any polyhedron [8–10]. In such a case computing cost can become demanding for large-scale models.

1.2. Cell Method: an alternative to FEM

A different strategy compared to previous approaches, which does not require evaluations of interpolating functions or local system matrix solutions, is here proposed and applied for discretization of 3-D piezoelectric problems on poly-meshes. Cell Method (CM) is alternative to FEM for the discretization of partial differential equations (PDEs) because field problem is formulated in a circuit-like manner in terms of DoFs such as line, surface, and volume integrals of scalar and vector fields, in one-to-one correspondence with geometric entities [11]. The CM has shown to be well suited for analyzing coupled problems, since topological relationships are split from constitutive relationships and integral variables are used to enforce element continuity. A coupling between different physics is provided in [12] by solving an electro-thermal problem with the CM. The extension of CM to elastic problems is more complex due to mathematical structure of elasticity, inherently different from electromagnetics. A first attempt of CM elastic formulation was proposed by Tonti for static problems [13] and for dynamic problems [14], proving that the same discrete gradient matrix of FEM could be obtained with CM. Using this discretization scheme, formulations for 2-D electro-elastic problems and 3-D electro-thermo-elastic problems were presented, respectively, in [15] and [16,17].

It was observed by Bossavit in [18] that the same discretization principles and techniques used by CM for computational electromagnetics could be used for coupled elasto-magnetic problems as well. In particular, it was shown that strain can be locally discretized by edge element functions, typically used in electromagnetic problems. These basis functions are related to edges and are useful to expand e.g. electric field in terms of edge DoFs (voltages), which is different from standard FEM formulations where nodal bases and nodal DoFs are used.

Starting from this standpoint, a CM-based approach for elasticity is here rigorously derived by splitting constitutive and topological relationships with a new set of variables, i.e. DoFs related to the displacement gradient instead of its symmetric part (strain). In such a way, piezoelectric problem can be discretized over polyhedral grids by using piecewise uniform bases [19], which have been applied up to now only to electromagnetic problems. The main advantage is that, unlike standard FEM, interpolation function evaluations on Gauss's points for numerical integration are not required and matrix assembly is completely Jacobian-free. Piecewise uniform basis functions are defined on star-shaped polyhedrons, with planar faces, and are therefore suitable for discretizing any type of model geometry.

1.3. Extending smoothing to CM

In standard FEM, once the displacement is assumed, its strain field is available using the strain-displacement relationship, which is called *fully-compatible strain field*. When low-order nodal functions are used, fully-compatible FEM leads to locking behavior of many problems. The discontinuous strain field at element interfaces induces inaccuracies in stress solutions. In addition, the Jacobian matrix related to domain mapping becomes badly conditioned on distorted elements, leading to further deterioration of solution accuracy [20]. To avoid low-order FEM issues, a numerical technique termed *Smoothed FEM* (S-FEM) was proposed in 2007 by Liu et al. [21,22]. S-FEM makes use of smoothing technique to modify the fully compatible strain field in order to avoid interface jumps between elements. The smoothed gradient matrix is obtained by

computing surface integrals on the boundary of smoothing cells, instead of volume integrals such as in standard FEM. In such a way, smoothed integration does not require an explicit computation of shape functions gradients nor physical-to-parental mapping, with benefits in terms of accuracy and simplicity in the numerical scheme. The type of smoothing technique (i.e. nodal, edge, face or cell-based smoothing) depends on the construction of smoothing domains, where strain field is piecewise uniform.

The extension of S-FEM to poly-FEM is quite recent and aims at combining advantages of both numerical techniques. In [23] a novel mesh carving approach, based on trimming and splitting processes on hexahedral meshes, is proposed. Trimmed hexahedra are replaced by polyhedrons and local stiffness matrices are obtained without explicitly computing nodal shape functions under the assumption of linear fields. For any polyhedral element, the number of local matrices to be computed is equal to the number of element boundary faces. This approach is then extended to non-linear elastic problems in [24], where a smoothed deformation gradient tensor for poly-meshes is defined. In [25] polyhedral elements are used as transition elements for coupling arbitrary non-matching hexahedral grids and smoothing is used for avoiding an explicit computation of nodal shape functions. Finally, a linear strain smoothing scheme is presented in [26] for improving accuracy of linear and quadratic approximations over convex polytopes. In this poly-FEM approach elementary stiffness matrix construction requires a number of submatrices equal to the number of elemental subcells times the number of Gauss's points per subcell. All previous approaches seem to be limited to elastic and single-material problems [22].

S-FEM has been extended to analyzing different types of multiphysics problems field such as acoustics [27], heat transfer [28], and metamaterials [29]. S-FEM for piezoelectric problems has been developed for 2-D models only [30,31]. In order to overcome shear locking arising when simulating thin structures (e.g., piezo-MEMS under bending) a novel smoothing technique is here developed and applied for the first time to CM, leading to the so-called *Smoothed Cell Method* (S-CM). Piecewise uniform bases are smoothed on face-based smoothing domains, which have octahedral shape and are constructed by linking any polygonal face to centroids of polyhedral cells attached to it. In such a way, only two elements per face are involved in the construction of smoothed stiffness matrix, differently from smoothed poly-FEMs presented above. Moreover, multi-material models (not yet considered by elastic poly-FEMs) can be treated as well by S-CM. Numerical examples show that S-CM results are comparable in terms of accuracy to second-order FEM on standard structured hexahedral meshes.

This paper is organized as follows. Differential formulations for 3-D piezoelectric static and dynamic problems are illustrated in Section 2. Piecewise uniform bases for poly-meshes together with Cell Method discretization of differential formulation are described in Section 3. The smoothing procedure applied to piecewise uniform bases is discussed in Section 4. Mesh generation and constitutive matrix assembly procedures are detailed in Section 5. Numerical results show that both standard and smoothed CM pass the patch test and that S-CM is accurate even when compared to second-order FEM on realistic MEMS models (Section 6). The outcomes of this research are finally drawn in the Conclusion.

2. Basic piezoelectric formulation

Let $\Omega \subset \mathbb{R}^3$ be a piezoelectric body with boundary $\Gamma = \partial\Omega$. Let Γ_s and Γ_f be parts of Γ with Dirichlet and Neumann boundary conditions (BCs), respectively. Displacement s_i is enforced on Γ_s and surface force density \bar{f}^i on Γ_f , with $i = 1, \dots, 3$ spatial component. The mechanical part of the solid response to an external body force density F^i is governed by dynamic equilibrium relationships, which expressed by Einstein's summation convention are [32]:

$$\begin{aligned} T_{/j}^{ij}(x) + F^i(x) &= \dot{p}^i(x), & x \in \Omega \\ T^{ij}(x) n_j(x) &= \bar{f}^i(x), & x \in \Gamma_f \end{aligned} \quad (1)$$

where T^{ij} are stress second-order tensor components, p^i are the momentum density components, $/j$ indicates the covariant derivative with respect to j -th spatial component, and n_j is the exterior unit normal on Γ , with $j = 1, \dots, 3$. By assuming small displacements, i.e. Ω is a linear electro-elastic solid, compatibility conditions become:

$$\begin{aligned} S_{ij}(x) &= \frac{S_{i/j}(x) + S_{j/i}(x)}{2}, & x \in \Omega \\ s_i(x) &= \bar{s}_i(x), & x \in \Gamma_s \end{aligned} \quad (2)$$

where S_{ij} are strain second-order tensor components and \bar{s}_i is the displacement imposed on the domain boundary.

For electrostatic problem in Ω similar relationships hold, i.e. Gauss's law and conservative electric field condition. Let Γ_ϕ be the part of the boundary with Dirichlet BCs (i.e. electric scalar potential ϕ) and Γ_σ that one with Neumann BCs (i.e. electric charge density σ), with $\Gamma = \Gamma_\phi \cup \Gamma_\sigma$. Electric equilibrium and compatibility become:

$$\begin{aligned} D_{/i}^i(x) &= 0, & x \in \Omega \\ D^i(x) n_i(x) &= -\sigma(x), & x \in \Gamma_\sigma \\ E_i(x) &= -\phi_{/i}(x), & x \in \Omega \\ \phi(x) &= \bar{\phi}(x), & x \in \Gamma_\phi \end{aligned} \quad (3)$$

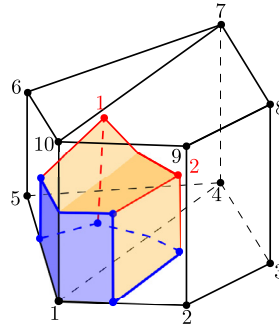


Fig. 1. Primal and dual grids with $N = \tilde{V} = 10$, $E = \tilde{F} = 17$, $F = \tilde{E} = 9$, $V = \tilde{N} = 2$ (nodes and edges of \mathcal{G}_Ω , $\tilde{\mathcal{G}}_\Omega$, and $\tilde{\mathcal{G}}_\Gamma$ are indicated in black, red, and blue color, respectively; nodes of \mathcal{G}_Ω are numbered from 1 to 10; nodes of $\tilde{\mathcal{G}}_\Omega$ from 1 to 2). (For interpretation of the colors in the figure(s), the reader is referred to the web version of this article.)

where D^i , E_i are the electric displacement and the electric field vector components, and $\bar{\phi}$ is the potential imposed on the domain boundary.

The electro-mechanical coupling is obtained in piezoelectric problems by constitutive relationships, relating displacements and electric potentials. By assuming piecewise homogeneous material properties and adopting the so-called *e-form* of constitutive equations, in which strain and electric field are used as independent variables, these equations can be written in the following form [33]:

$$\begin{aligned} T^{ij}(x) &= C_E^{ijkh}(x) S_{kh}(x) - e^{kij}(x) E_k(x), \\ D^i(x) &= e^{ikh}(x) S_{kh}(x) + \varepsilon_S^{ik}(x) E_k(x), \end{aligned} \quad (4)$$

where C_E^{ijkh} are the elastic fourth-order tensor components evaluated at constant electric field, e_{ikh} are the piezoelectric stress constant third-order tensor components, ε_S^{ik} are the dielectric constant second-order tensor components evaluated at constant strain, with spatial components $i, j, k, h = 1, \dots, 3$. Finally, momentum density is given by the following constitutive relationship:

$$p^i(x) = \rho(x) \kappa^{ij}(x) \dot{s}_j(x), \quad (5)$$

where ρ is the mass density and κ^{ij} are the metric tensor components.

3. Cell Method discretization

Unlike FEM formulations, where DoFs are related only to nodes and field equations are expressed in variational form, with the CM problem variables are defined on geometric entities, i.e. points, edges, faces, and volumes, and field equations are given directly in algebraic form suitable for computation [11]. A combinatorial model of the field problem is thus constructed. The computational domain Ω is first meshed into polyhedrons and the resulting mesh \mathcal{G}_Ω is termed *domain primal grid*, made of N vertexes, E edges, F faces, and V volumes (i.e. the number of polyhedral cells). The *boundary primal grid* \mathcal{G}_Γ is the restriction of \mathcal{G}_Ω to Γ , i.e. vertexes of \mathcal{G}_Γ are traces of bulk primal edges (of mesh \mathcal{G}_Ω), edges of \mathcal{G}_Γ are traces of bulk primal faces, and faces of \mathcal{G}_Γ are traces of bulk primal volumes [34]. Dual grids $\tilde{\mathcal{G}}_\Omega$ (made of \tilde{N} vertexes, \tilde{E} edges, \tilde{F} faces, and \tilde{V} volumes), and $\tilde{\mathcal{G}}_\Gamma$ (made of \tilde{N}_Γ vertexes, \tilde{E}_Γ edges, \tilde{F}_Γ faces) are then defined on Ω and Γ , respectively, by taking the barycentric subdivisions of primal grids \mathcal{G}_Ω and \mathcal{G}_Γ . In such a way, a one-to-one correspondence exists between primal and dual grids so that $\tilde{N} = V$, $\tilde{E} = F$, $\tilde{F} = E$, $\tilde{V} = N$. The *augmented dual grid* is then defined as the union of volume and boundary grids, as $\tilde{\mathcal{G}}_a = \tilde{\mathcal{G}}_\Omega \cup \tilde{\mathcal{G}}_\Gamma$ [34].

Fig. 1 shows an example of dual complexes for a mesh made up by a pair of polyhedrons $v_1 = \{1, 2, 3, 4, 10, 9, 8, 7\}$ and $v_2 = \{1, 4, 5, 6, 10, 7\}$. In that case, $N = \tilde{V} = 10$, $E = \tilde{F} = 17$, $F = \tilde{E} = 9$, and $V = \tilde{N} = 2$. Note that, for instance, the dual node 1 in red color (i.e. the centroid of v_1) is in one-to-one correspondence with v_1 ; the primal node 1 in black color is in one-to-one correspondence with the dual volume (shaded in orange) which is complemented by dual faces pertaining to $\tilde{\mathcal{G}}_\Gamma$ (shaded in blue).

Geometric entities of the primal grid are oriented by *inner* orientation, i.e. any vertex is oriented as a sink (inward direction of any edge connected to such vertex), any edge is oriented by taking its transversing direction from one end to the other, any face is oriented clockwise or counterclockwise, and any cell is an oriented volume by assuming all boundary faces oriented counterclockwise with respect to the exterior normal. The *outward* orientation of dual grid entities is inherited by the one-to-one correspondence with primal grid entities.

3.1. Discrete field variables (DoFs)

The orientation of geometric entities is useful to define DoFs properly, since these are defined as integrals of scalar or vector fields on lines, faces, volumes endowed with a specific orientation. These orientations can be regarded as local reference frames related to elements. For the mechanical problem, the following arrays of DoFs are defined for any i -th spatial component ($i = 1, \dots, 3$) and any time t : displacement on primal vertexes n , $\mathbf{s}_i(t) = (s_{i,n}(t))$; line integrals of the displacement gradient $R_{ij}(t) = s_{i/j}(t)$ along primal edges e , $\mathbf{r}_i(t) = (r_{i,e}(t))$, where $r_{i,e}(t) = \int_e R_{ij}(x, t) t^j(x) d\gamma_x$ and t^j is the unit tangent vector along e ; fluxes of the stress tensor through dual faces \tilde{f} , $\tilde{\mathbf{r}}^i(t) = (\tilde{r}_{\tilde{f}}^i(t))$, where $\tilde{r}_{\tilde{f}}^i(t) = \int_{\tilde{f}} T^{ij}(x, t) n_j(x) d\sigma_x$ and n_j is the unit normal vector to face \tilde{f} .

For the electrostatic problem, arrays of DoFs are as usual: electric potentials on primal nodes, $\Phi(t) = (\phi_n(t))$; voltages along primal edges, $\mathbf{u}(t) = (u_e(t))$, where $u_e(t) = \int_e E_j(x, t) t^j(x) d\gamma_x$ is the line integral of the electric field E_j ; fluxes of the electric displacement D_j through dual faces $\tilde{\mathbf{d}}(t) = (\tilde{d}_{\tilde{f}}(t))$, where $\tilde{d}_{\tilde{f}}(t) = \int_{\tilde{f}} D_j(x, t) n^j(x) d\sigma_x$.

3.2. Topological relations

An incidence number is +1 if a pair of connected geometric entities carries the same orientation, -1 otherwise, and 0 if they are disconnected. Connectivity between grid geometric entities is established by the following incidence matrices, with $\{0, \pm 1\}$ coefficients: \mathbf{G}_Ω (edges to nodes on \mathcal{G}_Ω), $\mathbf{D}_\Omega = -\mathbf{G}_\Omega^T$ (volumes to faces on $\tilde{\mathcal{G}}_\Omega$), and $\mathbf{D}_{\Omega\Gamma}$ (volumes on $\tilde{\mathcal{G}}_\Omega$ to faces on $\tilde{\mathcal{G}}_\Gamma$). On the primal grid, for the mechanical problem, line integrals of the displacement gradient are related to nodal displacements, whereas, for the electric problem, potentials are related to voltages by gradient theorem. Time dependence of DoFs arrays is omitted hereafter for the sake of brevity.

Let e be a primal edge oriented from vertex m to n . Mechanical and electric compatibility conditions (1) yield:

$$\begin{aligned} r_{i,e}(t) &= \int_e R_{ij}(x, t) t^j(x) d\gamma_x = \int_e s_{i/j}(x, t) t^j(x) d\gamma_x = s_{i,n}(t) - s_{i,m}(t), \\ u_e(t) &= \int_e E_j(x, t) t^j(x) d\gamma_x = \int_e -\phi_{/j}(x, t) t^j(x) d\gamma_x = \phi_m(t) - \phi_n(t), \end{aligned} \tag{6}$$

which, written in matrix form for all edges of \mathcal{G}_Ω , become:

$$\begin{aligned} \mathbf{r}_i &= \mathbf{G}_\Omega \mathbf{s}_i, \\ \mathbf{u} &= -\mathbf{G}_\Omega \Phi. \end{aligned} \tag{7}$$

On the augmented dual grid, mechanical and electric equilibrium are imposed by applying Gauss's theorem to any dual volume. By integrating (1) and recasting expression for all dual volumes of $\tilde{\mathcal{G}}_a$ in matrix form, the following system of second-order ordinary differential equations (ODEs) is obtained:

$$\begin{aligned} \tilde{\mathbf{D}}_\Omega \tilde{\mathbf{r}}^i + \tilde{\mathbf{D}}_{\Omega\Gamma} \tilde{\mathbf{r}}_\Gamma^i + \tilde{\mathbf{f}}^i &= \tilde{\mathbf{p}}^i, \\ \tilde{\mathbf{D}}_\Omega \tilde{\mathbf{d}} + \tilde{\mathbf{D}}_{\Omega\Gamma} \tilde{\mathbf{d}}_\Gamma &= \mathbf{0}, \end{aligned} \tag{8}$$

where $\tilde{\mathbf{r}}_\Gamma^i$ and $\tilde{\mathbf{d}}_\Gamma$ are, respectively, the array of stress tensor and electric displacement fluxes on the boundary dual faces, $\tilde{\mathbf{p}}^i = (\tilde{p}_{\tilde{v}}^i(t))$ are momentum integrals, and $\tilde{\mathbf{f}}^i = (\tilde{f}_{\tilde{v}}^i(t))$ are external body forces, both computed on dual volumes. Array coefficients $\tilde{p}_{\tilde{v}}^i(t) = \int_{\tilde{v}} p^i(x, t) dx$, $\tilde{f}_{\tilde{v}}^i(t) = \int_{\tilde{v}} \rho g^i(x, t) dx$ are integrals of momentum density and acceleration density $g^i(x, t)$, respectively, for any dual volume \tilde{v} .

3.3. Discrete constitutive relations

Constitutive equations (4) are not suited for building a CM formulation since the stress tensor is not naturally related to a geometric entity and thus does not depend directly on DoFs. By noting that strain tensor is $S_{kh}(x) = 1/2(R_{kh}(x) + R_{hk}(x))$ and that elasticity and piezoelectric tensors are symmetric, i.e. $C_E^{ijkh}(x) = C_E^{ijhk}(x)$ and $e^{ikh}(x) = e^{ihk}(x)$, constitutive equations for piecewise homogeneous materials can be reformulated as:

$$\begin{aligned} T^{ij}(x) &= C_E^{ijkh}(x) R_{kh}(x) - e^{kij}(x) E_k(x), \\ D^i(x) &= e^{ikh}(x) R_{kh}(x) + \varepsilon_S^{ik}(x) E_k(x). \end{aligned} \tag{9}$$

These relationships are discretized by using the so-called energetic approach in [19], where piecewise uniform vector basis functions for polyhedral meshes are provided. In such a way, discrete constitutive relationships are built from (9) in order to map DoFs on the augmented dual grid to the primal grid. These vector functions fulfill the following fundamental properties:

Please cite this article in press as: F. Moro et al., A face-smoothed cell method for static and dynamic piezoelectric coupled problems on polyhedral meshes, J. Comput. Phys. (2019), https://doi.org/10.1016/j.jcp.2019.02.012

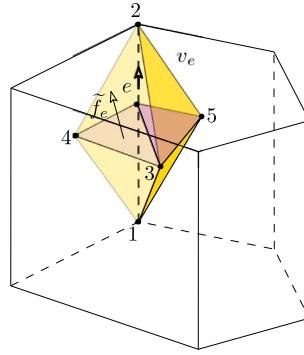


Fig. 2. Uniformity region and geometric entities for edge vector basis \mathbf{w}_e (for instance v_e , shaded in yellow, is the uniformity region related to edge e and is made up of (1234) and (1325) tetrahedrons; \tilde{f}_e , shaded in purple, is the dual face related to e).

- They form a vector basis (*linear independence*);
- An element-wise uniform vector field is exactly represented (*uniformity*);
- Dual geometric entities are mapped to primal ones (*consistency*);
- They enforce the continuity of field tangent component between polyhedral cells, whereas normal component can be discontinuous (*continuity*).

In (9) the stress tensor and the electric displacement fields are related (by integration) to DoFs defined on dual faces, whereas the displacement gradient tensor and the electric field are related to DoFs defined on primal edges. Therefore, an *edge vector basis functions* is required to map dual fluxes to primal line integrals by exploiting consistency and the assumption of a locally uniform field when mesh is sufficiently refined.

In the construction outlined in [19] the primal (polyhedral) cell v is first subdivided into tetrahedrons, by taking the centroid of v and the centroids of its faces. For any edge e' , the so-called *uniformity region* $v_{e'}$ within v is the union of tetrahedron pair attached to e' . In $v_{e'}$ the basis function \mathbf{w}_e is uniform. The union of subregions forms thus a partition of v , i.e. $v = \bigcup_{e'} v_{e'}$ and $v_{e'} \subseteq v$. The vector basis function related to e , restricted to any $v_{e'}$, is defined as:

$$\mathbf{w}_e(x) = \frac{\tilde{\mathbf{f}}_e}{\tilde{\mathbf{f}}_e \cdot \mathbf{e}} \delta_{ee'} + \left(\mathbf{I} - \frac{\tilde{\mathbf{f}}_{e'} \otimes \mathbf{e}'}{\tilde{\mathbf{f}}_{e'} \cdot \mathbf{e}'} \right) \frac{\tilde{\mathbf{f}}_e}{|v|}, \quad x \in v_{e'} \quad (10)$$

where, for instance, \mathbf{e} and $\tilde{\mathbf{f}}_e$ are edge and face vectors related to e and $\tilde{\mathbf{f}}_{e'}$, $\delta_{ee'}$ is the Kronecker delta ($\delta_{ee'} = 1$ if $e = e'$, 0 otherwise), \mathbf{I} is the identity tensor, $|v|$ is the cell volume, and \otimes is the dyadic product between vectors \mathbf{a} and \mathbf{b} , i.e. $(\mathbf{a} \otimes \mathbf{b}) \mathbf{c} = \mathbf{a} (\mathbf{b} \cdot \mathbf{c})$ for any vector \mathbf{c} . The edge function support is the union of all polyhedrons attached to edge e . Geometric entities involved in (10) are depicted in Fig. 2. The edge e is oriented from 1 to 2; the uniformity region v_e (shaded in yellow) is made up by tetrahedrons (1234) and (1325); dual face \tilde{f}_e , related to e , is shaded in purple.

Displacement gradient (for any k -th component) and electric field can be approximated, for any $x \in \Omega$ and time t , by the following expansions, under the assumption of locally uniform vector field with a very fine polyhedral mesh:

$$\begin{aligned} R_{kh}(x, t) &= \sum_{e=1}^E r_{k,e}(t) w_{h,e}(x), \\ E_k(x, t) &= \sum_{e=1}^E u_e(t) w_{k,e}(x), \end{aligned} \quad (11)$$

where, for instance, $w_{h,e}$ is the h -th Cartesian component of \mathbf{w}_e . Noting that consistency holds, i.e. $\int_{\Omega} \mathbf{w}_e(x) dx = \tilde{\mathbf{f}}_e$ for any edge e , and by assuming locally uniform fields, (9) can be expressed directly in terms of DoFs, as:

$$\begin{aligned} \tilde{t}_j^i(t) &= \int_{\tilde{f}} T^{ij}(x, t) n_j(x) d\sigma_x \\ &= \sum_{e=1}^E \int_{\Omega} C_E^{ijkh}(x) w_{j,e}(x) R_{kh}(x, t) - e^{kij}(x) w_{j,e}(x) E_k(x, t) dx, \end{aligned}$$

$$\begin{aligned} \tilde{d}^f(t) &= \int_{\tilde{f}} D^i(x, t) n_i(x) d\sigma_x \\ &= \sum_{e=1}^E \int_{\Omega} e^{ikh}(x) w_{i,e}(x) R_{kh}(x, t) + \varepsilon_S^{ik}(x) w_{i,e}(x) E_k(x, t) dx, \end{aligned} \tag{12}$$

which, by using (11), become:

$$\begin{aligned} \tilde{t}_f^i(t) &= \sum_{e=1}^E \sum_{e'=1}^E \int_{\Omega} C_E^{ijkh}(x) w_{j,e}(x) w_{h,e'}(x) r_{k,e'}(t) \\ &\quad - e^{kij}(x) w_{j,e}(x) w_{k,e'}(x) u_{e'}(t) dx, \\ \tilde{d}^f(t) &= \sum_{e=1}^E \sum_{e'=1}^E \int_{\Omega} e^{ikh}(x) w_{i,e}(x) w_{h,e'}(x) r_{k,e'}(t) \\ &\quad + \varepsilon_S^{ik}(x) w_{i,e}(x) w_{k,e'}(x) u_{e'}(t) dx. \end{aligned} \tag{13}$$

These constitutive relationships are assumed to hold, with a numerical approximation, even for non-locally uniform fields encountered in general problems. In matrix form discretized piezoelectric constitutive relationships (13) are:

$$\begin{aligned} \tilde{t}^i &= \mathbf{C}^{ik} \mathbf{r}_k - \mathbf{E}^{iT} \mathbf{u}, \\ \tilde{d} &= \mathbf{E}^k \mathbf{r}_k + \boldsymbol{\varepsilon} \mathbf{u}, \end{aligned} \tag{14}$$

where $\mathbf{C}^{ik} = (C_{ee'}^{ik})$, $\mathbf{E}^k = (E_{ee'}^k)$, $\boldsymbol{\varepsilon} = (\varepsilon_{ee'})$ are respectively the elastic, piezoelectric, and dielectric constitutive matrices with coefficients:

$$\begin{aligned} C_{ee'}^{ik} &= \int_{\Omega} C_E^{ijkh}(x) w_{j,e}(x) w_{h,e'}(x) dx, \\ E_{ee'}^k &= \int_{\Omega} e^{ikh}(x) w_{i,e}(x) w_{h,e'}(x) dx, \\ \varepsilon_{ee'} &= \int_{\Omega} \varepsilon_S^{ik}(x) w_{i,e}(x) w_{k,e'}(x) dx, \end{aligned} \tag{15}$$

with $e, e' = 1, \dots, E$ and $i, j, h, k = 1, \dots, 3$. These are complemented by momentum equation:

$$\tilde{\mathbf{p}}^i = \mathbf{M}_\rho \dot{\mathbf{s}}_i, \tag{16}$$

where $\mathbf{M}_\rho = (m_n)$ is the (diagonal) mass matrix. Its coefficients are obtained by integrating (5) over any dual cell \tilde{v}_n (in one-to-one correspondence to a primal node n) and noting that coefficients of array $\dot{\mathbf{s}}_i$ are given by evaluating the displacement at n . Since n is also the center of mass of \tilde{v}_n by definition, $m_n = \int_{\tilde{v}_n} \rho(x) dx$. With the assumption of a (locally) uniform mass density ρ_n , there are approximated as $m_n \approx \rho_n |\tilde{v}_n|$, where $|\cdot|$ indicates the cell volume. This approach leads to a construction of a *lumped mass matrix*, where mass is concentrated at the mesh nodes. A possible variation of the mass lumping approach, not here considered, is proposed in [35], with the so-called *Mass Redistributed FEM* (MR-FEM), even though applied to 2-D models discretized by linear triangular (T3) elements.

3.4. Static coupled problem

For the piezo-elastic case, by posing $\tilde{\mathbf{p}}^i = \mathbf{0}$ and by using (7) together with (14), matrix system (8) can be expressed in terms of displacements and electric potentials, as:

$$\begin{aligned} \mathbf{G}_\Omega^T \mathbf{C}^{ij} \mathbf{G}_\Omega \mathbf{s}_i - \mathbf{G}_\Omega^T \mathbf{E}^{iT} \mathbf{G}_\Omega \Phi &= \tilde{\mathbf{f}}^i + \tilde{\mathbf{D}}_{\Omega\Gamma} \tilde{\mathbf{t}}_\Gamma^i, \\ \mathbf{G}_\Omega^T \mathbf{E}^i \mathbf{G}_\Omega \mathbf{s}_i - \mathbf{G}_\Omega^T \boldsymbol{\varepsilon} \mathbf{G}_\Omega \Phi &= \tilde{\mathbf{D}}_{\Omega\Gamma} \tilde{\mathbf{d}}_\Gamma. \end{aligned} \tag{17}$$

The final electro-mechanical coupled system is derived from (17) by rearranging displacement components and electric potentials into a unique unknown array:

$$\begin{pmatrix} \mathbf{K}^{ij} & \mathbf{K}^{i\Phi} \\ \mathbf{K}^{i\Phi^T} & \mathbf{K}^{\Phi\Phi} \end{pmatrix} \begin{pmatrix} \mathbf{s}_i \\ \Phi \end{pmatrix} = \begin{pmatrix} \tilde{\mathbf{f}}^i + \tilde{\mathbf{D}}_{\Omega\Gamma} \tilde{\mathbf{t}}_\Gamma^i \\ \tilde{\mathbf{D}}_{\Omega\Gamma} \tilde{\mathbf{d}}_\Gamma \end{pmatrix}, \tag{18}$$

where $\mathbf{K}^{ij} = \mathbf{G}_\Omega^T \mathbf{C}^{ij} \mathbf{G}_\Omega$, $\mathbf{K}^{i\Phi} = -\mathbf{G}_\Omega^T \mathbf{E}^i \mathbf{G}_\Omega$, and $\mathbf{K}^{\Phi\Phi} = -\mathbf{G}_\Omega^T \boldsymbol{\epsilon} \mathbf{G}_\Omega$ are respectively the elastic, piezoelectric, dielectric stiffness matrices. By posing $\mathbf{x} = (\mathbf{s}_i, \Phi)^T$ and $\tilde{\mathbf{f}} = (\tilde{\mathbf{f}}^i + \tilde{\mathbf{D}}_{\Omega\Gamma} \tilde{\mathbf{t}}_\Gamma^i, \tilde{\mathbf{D}}_{\Omega\Gamma} \tilde{\mathbf{d}}_\Gamma)^T$ matrix system (18) becomes:

$$\mathbf{K} \mathbf{x} = \tilde{\mathbf{f}}, \tag{19}$$

which is solved after imposing nodal displacements (Dirichlet BCs) and tractions (Neumann BCs) on the boundary, and external body forces.

3.5. Dynamic coupled problem

Static Cell Method formulation for piezo-elasticity can be extended to dynamic problems by adding to equilibrium equations inertia forces and damping. As a reference problem, the case of a typical piezo-MEMS for energy harvesting is considered (e.g. Fig. 7 in Section 6.2). The mechanical base excitation and the piezoelectric material polarization are both directed along the 3-axis. Electrical charge is collected at circuit terminals, which are metallic layers placed at the bottom and upper faces of the piezo-layer (depicted in cyan in Fig. 7).

Frequency domain Let $g^i(x) = 0$ for any $i = 1, 2$ and $g^3(x, t) = g(x) \sin(\omega t)$ be the external acceleration density components, with $g(x)$ amplitude and ω angular frequency. Equation of motion (8) can be expressed in the frequency domain by posing $\tilde{\mathbf{f}} = \tilde{\mathbf{f}}_0 e^{i\omega t}$ and $\mathbf{s}_i = \mathbf{s}_{i,0} e^{i\omega t}$, where i is the imaginary unit. The hysteretic damping model is suitable for describing losses within elastic materials [36]. According to the hysteretic damping model, if the equation of motion is expressed in the frequency domain, the damping matrix is defined from the stiffness matrix as $\mathbf{D}^{ij} = i\eta \mathbf{K}^{ij}$, $i, j = 1, 2, 3$, where η is the so-called *isotropic loss factor* (to be determined experimentally). External circuit conditions have to be introduced as well for modeling piezo-energy harvesters. External voltage source Φ_{ext} , connected to cantilever terminals, is related to terminal electrical charge σ by Ohm's law, i.e. $\Phi_{ext} = R_{ext} \dot{\sigma}$ with R_{ext} load resistance. Electrical charge affects the electrostatic problem according to (18).

Dynamic behavior of the coupled piezoelectric problem in discrete form is governed by the following equation:

$$(-\omega^2 \mathbf{M} + i\omega \mathbf{C} + \mathbf{D} + \mathbf{K}') \mathbf{x}_0 = \tilde{\mathbf{f}}_0, \tag{20}$$

where $\mathbf{x}_0 = (\mathbf{s}_{i,0}, \Phi_0, \sigma)^T$, $\tilde{\mathbf{f}}_0 = (\tilde{\mathbf{f}}_0^i + \tilde{\mathbf{D}}_{\Omega\Gamma} \tilde{\mathbf{t}}_{\Gamma 0}^i, \tilde{\mathbf{D}}_{\Omega\Gamma} \tilde{\mathbf{d}}_{\Gamma 0}, 0)^T$ are complex vectors. Matrices in (20) are defined as:

$$\mathbf{M} = \begin{pmatrix} \mathbb{I}_3 \otimes \mathbf{M}_\rho & \mathbb{O} \\ \mathbb{O} & \mathbb{O} \end{pmatrix}, \quad \mathbf{C} = \begin{pmatrix} \mathbb{O} & \mathbb{O} \\ \mathbb{O} & R_{ext} \end{pmatrix},$$

$$\mathbf{D} = \begin{pmatrix} \mathbf{D}^{ij} & \mathbb{O} \\ \mathbb{O} & \mathbb{O} \end{pmatrix}, \quad \mathbf{K}' = \begin{pmatrix} \mathbf{K}^{ij} & \mathbf{K}^{i\Phi} & \mathbb{O} \\ \mathbf{K}^{i\Phi T} & \mathbf{K}^{\Phi\Phi} & \mathbf{K}^{\Phi\sigma} \\ \mathbb{O} & \mathbf{K}^{\Phi\sigma T} & \mathbb{O} \end{pmatrix},$$

where \mathbb{I}_3 is a 3×3 identity matrix, \mathbb{O} are null matrices, and $\mathbf{K}^{\Phi\sigma} = (0, \dots, -1, \dots, 0)^T$, with -1 corresponding to position of Φ_{ext} within potential array Φ_0 .

Time domain Hysteretic damping is not defined for transient analysis models, therefore Rayleigh's model is used as an equivalent proportional damping model [36]. According to Rayleigh's theory damping matrices are defined as a linear combination of mass and stiffness matrices, that is $\mathbf{D}^{ij} = \alpha \mathbf{M}_\rho + \beta \mathbf{K}^{ij}$, where α and β are coefficients to be defined experimentally.

The dynamic behavior of piezoelectric body is then governed by the following second-order ODE system:

$$\mathbf{M} \ddot{\mathbf{x}} + (\mathbf{C} + \mathbf{D}) \dot{\mathbf{x}} + \mathbf{K} \mathbf{x} = \tilde{\mathbf{f}}, \tag{21}$$

which is solved by the Newmark- β integration scheme, described as follows. The responses after time Δt , i.e. \mathbf{x}_{n+1} , $\dot{\mathbf{x}}_{n+1}$, $\ddot{\mathbf{x}}_{n+1}$, are calculated from those at the previous n -th time step, i.e. \mathbf{x}_n , $\dot{\mathbf{x}}_n$, $\ddot{\mathbf{x}}_n$, and from the rhs $\tilde{\mathbf{f}}_n$, as

$$\mathbf{A} \ddot{\mathbf{x}}_{n+1} = \mathbf{b}_{n+1},$$

$$\dot{\mathbf{x}}_{n+1} = \dot{\mathbf{x}}_n + (1 - \gamma) \Delta t \ddot{\mathbf{x}}_n + \gamma \Delta t \ddot{\mathbf{x}}_{n+1},$$

$$\mathbf{x}_{n+1} = \mathbf{x}_n + \Delta t \dot{\mathbf{x}}_n + \Delta t^2 \left[\left(\frac{1}{2} - \beta \right) \ddot{\mathbf{x}}_n + \beta \ddot{\mathbf{x}}_{n+1} \right], \tag{22}$$

where

$$\mathbf{A} = \mathbf{M} + \gamma \Delta t \mathbf{D} + \xi \Delta t^2 \mathbf{K},$$

$$\mathbf{b}_{n+1} = \tilde{\mathbf{f}}_{n+1} - \mathbf{K} \mathbf{x}_n - (\mathbf{D} + \Delta t \mathbf{K}) \dot{\mathbf{x}}_n - \left[(1 - \gamma) \Delta t \mathbf{D} + \Delta t^2 \left(\frac{1}{2} - \xi \right) \mathbf{K} \right] \ddot{\mathbf{x}}_n. \tag{23}$$

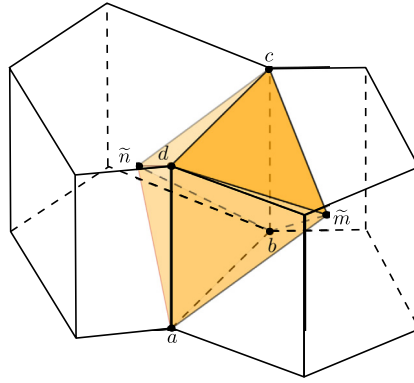


Fig. 3. Face-based smoothing domain: two polyhedral cells are attached to primal face $f = (abcd)$; the smoothing domain related to f (region shaded in color, with octahedral shape) is the union of pyramids with base f and apexes \tilde{m} , \tilde{n} .

The iterative time-stepping integration algorithm is proven to be unconditionally stable and convergent for a proper choice of parameters γ and ξ such that $4\beta \geq 2\gamma \geq 1$ [37].

4. Polyhedral face-smoothed functions

The idea of shape function *smoothing* has been introduced first in the context of mesh-free methods by Chen [38] and then extended by Liu et al. [39] in order to overcome some peculiar issues of low-order finite element elements when applied to elasticity problems. In particular the standard FEM formulation with first-order Lagrange elements for hexahedral or tetrahedral meshes leads to shear and/or volume locking. The assumed continuous displacement field provides a discontinuous strain field across element interfaces and, in turn, a poor numerical accuracy. This holds true in particular for low-order hexahedral elements, which are suitable for discretization of thin layered and Manhattan structures. Likewise hexahedral finite elements also edge elements for polyhedral cells, presented in Section 3.3, suffer from locking because the normal component of displacement gradient jumps across elements. To overcome this issue, smoothing is here extended to piecewise uniform edge vector functions.

In the face-based smoothed finite element method (FS-FEM), presented in [40] for tetrahedral elements, the domain discretization is the same as that of standard FEM, but the integration using the strain-smoothing technique is performed over smoothing domains constructed over element faces. Up to now FS-FEM has not been developed for polyhedral meshes, even though the construction of smoothing domain is much simpler (i.e. only a pair of polyhedrons involved for polygonal face). The *face smoothing* approach is here extended to polyhedral cells in the CM framework. Moreover, multi-material models can be treated as well by the proposed smoothing strategy for polyhedral meshes, following a strategy similar to that one presented in [31] for NS-FEM on triangular meshes and in [41] for ES-FEM on triangular/tetrahedral meshes.

In order to obtain a *local integral approximation* of \mathbf{F} the computational domain Ω is partitioned into subdomains Ω_μ with homogeneous material μ . Each subdomain is divided into a number of non-overlapping smoothing cells \hat{v}_f equal to the number of primal faces F . For any face f , \hat{v}_f is the union of pyramids with base f and apexes the centroids of primal cells sharing f . The resulting mesh, obtained from the primal grid \mathcal{G}_Ω , is the *smoothing grid* $\hat{\mathcal{G}}_\Omega = \bigcup_f \hat{v}_f$, with $\hat{v}_f \cap \hat{v}_{f'} = \emptyset$ for any $f \neq f'$. By this construction the original domain Ω is thus entirely paved by smoothing cells.

Fig. 3 shows an example of \hat{v}_f for an interior face; smoothing cells related to boundary faces are made up by one pyramid only.

The *smoothed field* is defined on the top of the smoothing grid, following the definitions of smoothed strain provided for FS-FEM, see e.g. [42] equation (30) or [40] equation (7). Using notations above, it can be written:

Definition 1 (Smoothed field). Let \mathbf{F} be a generic scalar, vector, or tensor field defined on domain Ω . If $x \in \hat{\mathcal{G}}_\Omega$ then there exists f such that $x \in v_f$, and \mathbf{F} can be approximated locally as a uniform field

$$\hat{\mathbf{F}}(x) = \frac{1}{|\hat{v}_f|} \int_{\hat{v}_f} \mathbf{F}(y) dy.$$

The resulting field $\hat{\mathbf{F}}$ is defined directly on the smoothing grid and is a piecewise uniform approximation of the original field \mathbf{F} .

Definition 2 (Smoothed edge functions). For any face f and edge e , the smoothed vector functions $\hat{\mathbf{w}}_e$ are the integral approximations of piecewise uniform vector bases \mathbf{w}_e , i.e. $\hat{\mathbf{w}}_e(x) = \frac{1}{|\hat{v}_f|} \int_{\hat{v}_f} \mathbf{w}_e(y) dy$, $x \in \hat{v}_f$, such that

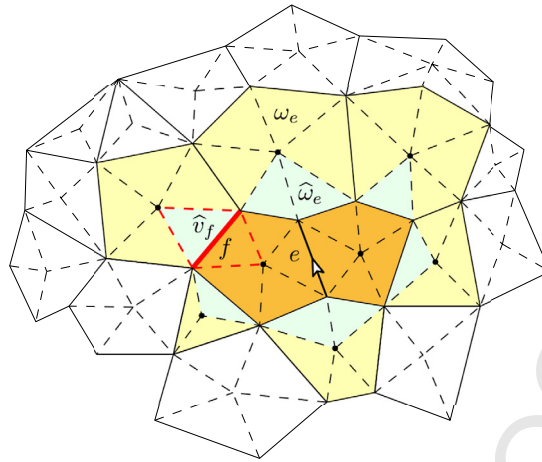


Fig. 4. Smoothed edge function support $\widehat{\omega}_e$ obtained by smoothing basis vector \mathbf{w}_e on a polygonal mesh ($\widehat{\omega}_e$, in cyan, is the union of smoothing cells \widehat{v}_f overlapping $\text{supp}(\mathbf{w}_e)$, in orange; $\widehat{\omega}_e$ is included in the uniformity region ω_e , in yellow).

1. $\int_{\widehat{v}_f} \widehat{\mathbf{w}}_e(x) dx = \int_{\widehat{v}_f} \mathbf{w}_e(x) dx$;
2. $\widehat{\mathbf{w}}_e$ is uniform within \widehat{v}_f .

Let $\text{supp}(\mathbf{w}_e)$ be the support of \mathbf{w}_e , i.e. the union of polyhedral cells attached to e . The support of $\widehat{\mathbf{w}}_e$ is then provided by the union of all smoothing cells intersecting $\text{supp}(\mathbf{w}_e)$, i.e. $\widehat{\omega}_e = \text{supp}(\widehat{\mathbf{w}}_e) = \bigcup_f \widehat{v}_f$ such that $\widehat{v}_f \cap \text{supp}(\mathbf{w}_e) \neq \emptyset$. Finally, let ω_e be the minimal union of polyhedral cells containing $\widehat{\omega}_e$.

For the sake of simplicity, Fig. 4 provides an example of this construction for a two-dimensional polygonal mesh. For any edge e (indicated by an arrow), the corresponding smoothed function support is built according to these steps:

1. $\text{supp}(\mathbf{w}_e)$ is the union of pair of polygons (in orange) attached to e ;
2. Polygon vertexes are joined to their centroids in order to build a secondary mesh (in dashed black line);
3. For any face f (in red line), the corresponding smoothing domain \widehat{v}_f is the union of triangles of secondary mesh attached to f (in dashed red line);
4. $\widehat{\omega}_e$ is the union of smoothing domains covering $\text{supp}(\mathbf{w}_e)$ (in cyan);
5. ω_e is the union of polygons covering $\widehat{\omega}_e$ (in yellow).

The extension of this construction to a 3-D mesh made up of polyhedrons is then trivial. Note that, in that case, $\text{supp}(\mathbf{w}_e)$ can be the union of more than two polyhedrons, unlike a 2-D mesh, and v_f is the union of a pair of pyramids with polygonal base f as depicted in Fig. 3.

Property 1 (Uniformity). Any uniform vector field \mathbf{a} in ω_e can be expressed within $\widehat{\omega}_e \subset \omega_e$ as a function of its edge DoFs, i.e. $a_{e'} = \int_{e'} \mathbf{a}(x) \cdot \mathbf{t}(x) d\gamma_x$, as:

$$\mathbf{a}(x) = \sum_{e' \in \mathcal{E}(\omega_e)} \widehat{\mathbf{w}}_{e'}(x) a_{e'}, \quad x \in \widehat{\omega}_e \tag{24}$$

where $\mathcal{E}(\omega_e)$ is the set of all primal edges within \mathcal{G}_Ω pertaining to ω_e .

Proof. Any uniform field can be exactly represented as $\mathbf{a}(x) = \sum_{e'} \mathbf{w}_{e'}(x) a_{e'}$, for any $x \in \omega_e$, by using piecewise uniform edge basis functions (10). If \mathbf{a} is uniform within ω_e , then is uniform also within its subset $\widehat{\omega}_e$ and $\mathbf{a}(x) = \widehat{\mathbf{a}}(x)$ for any $x \in \widehat{\omega}_e$. By using Definition 1, the corresponding smoothed field becomes:

$$\widehat{\mathbf{a}}(x) = \frac{1}{|\widehat{v}_f|} \int_{\widehat{v}_f} \mathbf{a}(x) dx = \sum_{e' \in \mathcal{E}(\omega_e)} \widehat{\mathbf{w}}_{e'}(x) a_{e'}. \quad \square \tag{25}$$

Property 2 (Consistency). For any edge e , let $\tilde{\mathbf{f}}_e$ be the area vector related to dual face \tilde{f}_e and $\Omega_\mu \subseteq \Omega$ a subdomain with homogeneous material μ , where bases \mathbf{w}_e are defined. Then, the following geometric property holds:

$$\int_{\Omega_\mu} \widehat{\mathbf{w}}_e(x) dx = \tilde{\mathbf{f}}_e. \tag{26}$$

Proof. By splitting the computational domain into smoothing regions \widehat{v}_f and exploiting the consistency property of edge vector bases \mathbf{w}_e , Definition 2 provides:

$$\int_{\Omega_\mu} \widehat{\mathbf{w}}_e(x) dx = \sum_{f \in \mathcal{F}(\Omega_\mu)} \int_{\widehat{v}_f} \widehat{\mathbf{w}}_e(x) dx = \sum_{f \in \mathcal{F}(\Omega_\mu)} \int_{\widehat{v}_f} \mathbf{w}_e(x) dx = \int_{\Omega_\mu} \mathbf{w}_e(x) dx = \widetilde{\mathbf{f}}_e, \tag{27}$$

where $\mathcal{F}(\Omega_\mu)$ is the set of all primal faces within \mathcal{G}_Ω pertaining to Ω_μ . \square

Exploiting previous properties **the following result show that, for** uniform fields, an exact reconstruction of fluxes (on the dual complex) can be obtained from line integrals (on the primal complex). This property makes it possible to build approximate constitutive relationships for CM by using smoothed edge functions instead of standard piecewise uniform edge vector bases.

The construction of discrete constitutive equations is similar to (13) and is here reported for a fourth-order tensor, e.g. elasticity tensor C_E^{ijkl} in (4). Similar derivations hold for discretizing piezoelectric and dielectric tensors. These matrix relationships are built and assembled separately on each subdomain Ω_μ with homogeneous material properties, in order to fulfill Property 2. This extends smoothing to multi-material problems discretized by poly-meshes.

Property 3 (Smoothed constitutive relationship). Let a_{kh}, b^{ij} be locally uniform tensor fields in ω_e and τ^{ijkl} a tensor describing homogeneous material properties in $\Omega_\mu \subseteq \Omega$, with $b^{ij} = \tau^{ijkl} a_{kh}$ local constitutive relationship and $i, j, k, h = 1, 2, 3$ indexes of spatial components. For any pair (i, k) , the corresponding discrete constitutive relationship is a matrix τ^{ik} with coefficients:

$$\tau_{ee'}^{ik} = \int_{\Omega_\mu} \tau^{ijkl}(x) \widehat{w}_{j,e}(x) \widehat{w}_{h,e'}(x) dx. \tag{28}$$

Then, fluxes of b^{ij} through dual faces are exactly reconstructed from line integrals of a_{kh} along primal edges, as

$$\widetilde{b}_e^i = \sum_{e' \in \mathcal{E}(\omega_e)} \tau_{ee'}^{ik} a_{k,e'}. \tag{29}$$

Proof. Let $a_{k,e'} = \int_{e'} a_{kh}(x) t^h(x) d\gamma_x$ be the line integral of a_{kh} related to edge e' . Let $\widetilde{b}_e^i = \int_{\widetilde{f}_e} b^{ij}(x) n_j(x) d\sigma_x$ the flux of b^{ij} through the dual face \widetilde{f}_e related to edge e . By noting that $\widehat{\omega}_e$ is the support of $\widehat{\mathbf{w}}_e$, the following identities hold:

$$\begin{aligned} \sum_{e' \in \mathcal{E}(\Omega_\mu)} \tau_{ee'}^{ik} a_{k,e'} &= \int_{\Omega_\mu} \tau^{ijkl}(x) \widehat{w}_{j,e}(x) \widehat{w}_{h,e'}(x) a_{k,e'} dx \\ &= \sum_{e' \in \mathcal{E}(\omega_e)} \int_{\Omega_\mu} \tau^{ijkl}(x) \widehat{w}_{j,e}(x) \widehat{w}_{h,e'}(x) a_{k,e'} dx \\ &= \sum_{e' \in \mathcal{E}(\omega_e)} \int_{\widehat{\omega}_e} \tau^{ijkl}(x) \widehat{w}_{j,e}(x) \widehat{w}_{h,e'}(x) a_{k,e'} dx, \end{aligned}$$

which, by noting that $\widehat{\omega}_e \subset \omega_e$ and $a_{kh}(x) = \sum_{e' \in \mathcal{E}(\omega_e)} a_{k,e'} \widehat{w}_{h,e'}(x)$ in ω_e , becomes:

$$\int_{\widehat{\omega}_e} \tau^{ijkl}(x) \widehat{w}_{j,e}(x) a_{kh}(x) dx = \int_{\widehat{\omega}_e} \widehat{w}_{j,e}(x) b^{ij}(x) dx.$$

Due to uniformity of b^{ij} in $\widehat{\omega}_e$ and to consistency property of $\widehat{\mathbf{w}}_e$ in Ω_μ :

$$\begin{aligned} \int_{\widehat{\omega}_e} \widehat{w}_{j,e}(x) b^{ij}(x) dx &= \left(\int_{\widehat{\omega}_e} \widehat{w}_{j,e}(x) dx \right) b^{ij}(x) = \left(\int_{\Omega_\mu} \widehat{w}_{j,e}(x) dx \right) b^{ij}(x) \\ &= \widetilde{f}_{j,e} b^{ij}(x) = \int_{\widetilde{f}_e} b^{ij}(x) n_j(x) d\sigma_x = \widetilde{b}_e^i. \quad \square \end{aligned}$$

In such a way, piezoelectric constitutive relationships (9) can be discretized following the same strategy used to obtain (13), that is

$$\begin{aligned}\tilde{\mathbf{t}}_f^i(t) &= \sum_{e=1}^E \sum_{e'=1}^E \int_{\Omega} C_E^{ijkh}(x) \widehat{w}_{j,e}(x) \widehat{w}_{h,e'}(x) r_{k,e'}(t) - e^{kij}(x) \widehat{w}_{j,e}(x) \widehat{w}_{k,e'}(x) u_{e'}(t) dx, \\ \tilde{\mathbf{d}}_f^i(t) &= \sum_{e=1}^E \sum_{e'=1}^E \int_{\Omega} e^{ikh}(x) \widehat{w}_{i,e}(x) \widehat{w}_{h,e'}(x) r_{k,e'}(t) + \varepsilon_S^{ik}(x) \widehat{w}_{i,e}(x) \widehat{w}_{k,e'}(x) u_{e'}(t) dx.\end{aligned}\quad (30)$$

In matrix form these constitutive relationships become:

$$\begin{aligned}\tilde{\mathbf{t}}^i &= \widehat{\mathbf{C}}^{ik} \mathbf{r}_k - \widehat{\mathbf{E}}^{iT} \mathbf{u}, \\ \tilde{\mathbf{d}} &= \widehat{\mathbf{E}}^k \mathbf{r}_k + \widehat{\boldsymbol{\varepsilon}} \mathbf{u},\end{aligned}\quad (31)$$

where $\widehat{\mathbf{C}}^{ik} = (\widehat{C}_{ee'}^{ik})$, $\widehat{\mathbf{E}}^k = (\widehat{E}_{ee'}^k)$, $\widehat{\boldsymbol{\varepsilon}} = (\widehat{\varepsilon}_{ee'})$ are respectively the elastic, piezoelectric, and dielectric *smoothed constitutive matrices* with coefficients:

$$\begin{aligned}\widehat{C}_{ee'}^{ik} &= \int_{\Omega} C_E^{ijkh}(x) \widehat{w}_{j,e}(x) \widehat{w}_{h,e'}(x) dx, \\ \widehat{E}_{ee'}^k &= \int_{\Omega} e^{ikh}(x) \widehat{w}_{i,e}(x) \widehat{w}_{h,e'}(x) dx, \\ \widehat{\varepsilon}_{ee'}^{ik} &= \int_{\Omega} \varepsilon_S^{ik}(x) \widehat{w}_{i,e}(x) \widehat{w}_{k,e'}(x) dx,\end{aligned}\quad (32)$$

with $e, e' = 1, \dots, E$ and $i, j, h, k = 1, \dots, 3$.

5. Numerical implementation

5.1. Polyhedral mesh generation

Since commercial software for mesh generation provides mostly tetrahedral or hexahedral meshes, a polyhedral mesh generator based on the concept of mesh carving has been developed and coded in Matlab[®] software environment. The polyhedral mesh generator is suitable for discretizing thin multi-layered structures of any shape, which are typical of piezoelectric MEMS devices.

Mesh generation steps are schematically depicted in Fig. 5. A 2-D structured mesh of quadrilateral cells is first built (Fig. 5a). Any row of matrix **nod2d** is a pair of vertex (x, y) Cartesian coordinates. 2-D polygonal mesh is represented by a cell-array data structure **poly**, in which any entry is a list of four vertex indexes (i.e. quadrilateral). After mesh clipping a polygonal mesh with curved boundaries is generated (Fig. 5b). Polygonal cells can be deleted by *deletepolygons* algorithm. Any entry of **poly** represents a generic polygon with an arbitrary number of vertexes. The 3-D polyhedral mesh is built from 2-D mesh (Fig. 5c) by sweeping. 3-D mesh can be carved by using *deletepolyhedra* algorithm for deleting a list of polyhedral cells (Fig. 5d). Clipping and sweeping algorithms are detailed below.

The quadrilateral mesh is clipped by Algorithm 1 (Appendix A), which is useful for finding intersections with circles (curved boundary edges). Any polygonal cell **polygon** is clipped by the function *polyintersect_circle*, which finds the intersection **vert** between **polygon** and a circle of radius R and center (x_C, y_C) . The intersection is analytically computed in order to avoid round-off errors, which can lead to robustness issues in the algorithm. Array **vert** is made by a pair of vertexes **vert**(1), **vert**(2), which may overlap in case. Vertexes are considered to be overlapping for a given tolerance, which is computed from the convex hull of the polygonal mesh. By clipping polygon with the edge passing through intersection vertexes, a pair of counter-clockwise oriented curves **curve**[1], **curve**[2] is generated. New polygons created by mesh clipping (which can be non-convex) are added to cell list **poly**. The final polygonal mesh is made up of N_{2d} vertexes, E_{2d} edges, and F_{2d} polygons.

Input data for the sweeping algorithm are incidence matrices of polygonal mesh, the coordinate matrix, and the sweeping direction. Primal edge-to-vertex incidence matrix \mathbf{G}_{2d} (of size $E_{2d} \times N_{2d}$) has coefficient $\mathbf{G}_{2d}(e, n) = +1$ if edge e enters vertex n , -1 otherwise. Face-to-edge incidence matrix \mathbf{C}_{2d} (of size $F_{2d} \times E_{2d}$) has coefficient $\mathbf{C}_{2d}(f, e) = +1$ if polygon boundary f is oriented according to edge e , -1 otherwise. For horizontal edges and faces incidence numbers do not change for any value of **vecz**, whereas for vertical ones these can be easily reconstructed from 2-D matrices. The sweeping direction (z-axis) is orthogonal to the base (x, y) -plane with 2-D mesh. Sweeping coordinates (one coordinate for each 3-D mesh layer) are in the array **vecz** of length N_z . 3-D mesh elements have the following sizes: $N_{3d} = N_{2d} N_z$ vertexes, $E_{3d} = E_{2d} N_z + N_{2d} (N_z - 1)$ edges, $F_{3d} = F_{2d} N_z + E_{2d} (N_z - 1)$ faces, $V_{3d} = F_{2d} (N_z - 1)$ polyhedral cells.

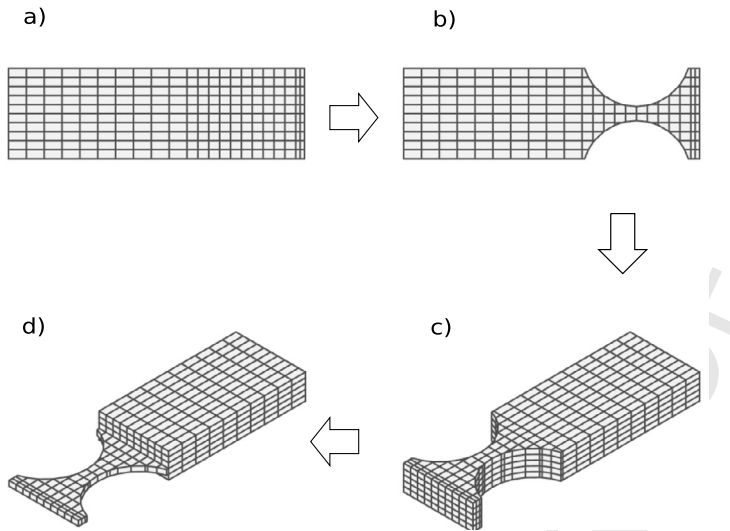


Fig. 5. Polyhedral mesh generation by clipping and sweeping a 2-D polygonal mesh.

Polyhedral mesh is generated from 2-D incidence matrices and the sweeping array as follows. 3-D incidence matrices \mathbf{G}_{3d} ($E_{3d} \times N_{3d}$), \mathbf{C}_{3d} ($F_{2d} \times E_{2d}$), \mathbf{D}_{3d} ($V_{3d} \times F_{3d}$) and coordinate matrix **nod3d**, made of (x, y, z) -triplets for any vertex, are first built from corresponding 2-D matrices. Cell-array data structures **edgs**, **facs**, **cells** (representing edges, polygonal faces, and polyhedral cells) are then reconstructed from element connectivities by Matlab® commands for sparse matrices. Edges, faces, and cells are oriented according to inner orientation assigned to primal grid. This procedure is described by Algorithm 2 (Appendix A), where \mathbb{I}_s indicates the identity matrix of size s and $find(\mathbf{v})$ command gives indexes of non-zero entries of an array \mathbf{v} .

5.2. Constitutive matrix assembly

Assembly procedures for standard and smoothed discrete constitutive relationships are presented. The assembly process for linear elastic materials is similar to piezoelectric ones. For any domain Ω_μ , with homogeneous material properties, assembly procedure is repeated. Input data are coordinate matrix **nod3d**, data structures **edgs**, **facs**, **cells** and the material property matrix. Constitutive relationships (4) are rewritten in Voigt's notation for representing second-order tensors as vectors and third and fourth-order tensors as matrices, with the following maps: $11 \rightarrow 1, 22 \rightarrow 2, 33 \rightarrow 3, 13 \rightarrow 4, 23 \rightarrow 5, 12 \rightarrow 6$. In this way the dielectric matrix ϵ_S is diagonal for typical piezoelectric materials and the piezoelectric coupling matrix reduces to:

$$\mathbf{e} = \begin{pmatrix} 0 & 0 & 0 & 0 & 0 & e_{15} & 0 \\ 0 & 0 & 0 & 0 & e_{24} & 0 & 0 \\ e_{31} & e_{32} & e_{33} & 0 & 0 & 0 & 0 \end{pmatrix}, \quad (33)$$

while the symmetric elastic stiffness matrix results:

$$\mathbf{c}_E = \begin{pmatrix} C_{11} & C_{12} & C_{13} & 0 & 0 & 0 \\ C_{12} & C_{22} & C_{23} & 0 & 0 & 0 \\ C_{13} & C_{23} & C_{33} & 0 & 0 & 0 \\ 0 & 0 & 0 & C_{44} & 0 & 0 \\ 0 & 0 & 0 & 0 & C_{55} & 0 \\ 0 & 0 & 0 & 0 & 0 & C_{66} \end{pmatrix}. \quad (34)$$

These matrices are stored in an array format for tensors in the material property matrix, equivalent to (4):

$$\mathbf{m} = \begin{pmatrix} \mathbf{c}_E & -\mathbf{e}^T \\ \mathbf{e} & \epsilon_S \end{pmatrix}. \quad (35)$$

The assembly procedure based on standard CM discretization is schematically described in Algorithm 3 (Appendix A). For any polygon/polyhedron, its area/volume $vol(\cdot)$ and centroid $centre(\cdot)$ are computed by algorithms proposed in [43], with exploit divergence theorem to reduce complexity. Any polyhedron face is represented as a cell-array of edge indexes indicated with **face**. Any polyhedron is represented as a cell-array of face indexes indicated with **cell**. **edgs** is the cell-array of polyhedron edges, where any entry **edge** is an oriented pair of vertexes indexes. The array of global edge indexes (as

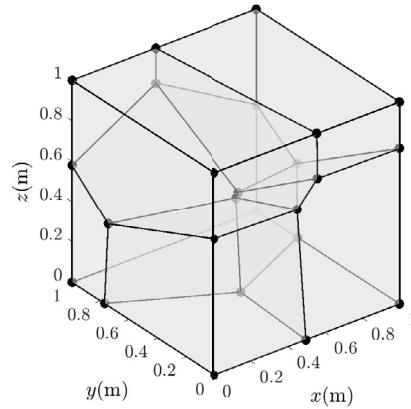


Fig. 6. Polyhedral mesh used for the patch test.

stored in the cell-array **edgs**) is indicated with **iedgs**. In order to calculate basis functions, for any edge **ts** corresponding edge vector **e** and dual face area vector $\tilde{\mathbf{f}}_e$ are calculated. For any edge, cell-array **edgtfac** provides faces attached to that edge and **supp** the volume of the corresponding uniformity region (Fig. 2). Edge functions \mathbf{w}_e are computed by function *basis*(·), which implements definition (10), and are stored as $E_v \times 3$ size matrices, where E_v is the local number of edges (i.e. uniformity regions). Mapping function *map*(·) extracts tensor coefficients from **m**, restoring original format of system (4). Integral for coefficients in (15) are finally computed without need of evaluating Jacobian, unlike FEM, and assembled in the global constitutive matrix **mat**.

Constitutive matrix assembly in the case of smoothed CM is based on faces instead of cells, differing thus from standard CM or FEM assembly (Algorithm 4, Appendix A). For any face **smoothface** adjacent polyhedrons **adjcells** are identified by the cell-array **facetocells**. For internal cells two polyhedrons are selected, whereas only one polyhedron for boundary cells. For any adjacent cell v , the volume **svol**[v][e] of the intersection between the smoothing cell \hat{v}_f (diamond shaped region of Fig. 3) and the uniformity region v_e related to edge e is calculated. The smoothed vector function $\tilde{\mathbf{w}}_e$ is a cell-array structure, where any entry $\tilde{\mathbf{w}}_e[v]$ is a $E_v \times 3$ matrix. According to Definition (2), it is obtained by first averaging edge basis function \mathbf{w}_e on $\hat{v}_f \cap v$ and then on cell \hat{v}_f .

6. Numerical results

6.1. 3-D piezoelectric patch test

In order to validate polyhedral CM with edge vector basis functions (poly-CM) for static problems and that one with smoothed edge vector functions (poly-SCM) a linear patch test is proposed. A unit cube made of piezoelectric material (PZT-5H in Table B.2, Appendix B) is meshed in non-regular polyhedrons as depicted in Fig. 6. By assuming Dirichlet BCs on the whole boundary, displacements u, v, w and potential φ are assumed to be in the whole domain:

$$\begin{aligned} u(x, y, z) &= 0.1 + 0.1x + 0.2y + 0.2z, \\ v(x, y, z) &= 0.05 + 0.015x + 0.1y + 0.2z, \\ w(x, y, z) &= 0.05 + 0.1x + 0.2y + 0.2z, \\ \varphi(x, y, z) &= u(x, y, z) + v(x, y, z) + w(x, y, z), \end{aligned} \quad (36)$$

where x, y, z are Cartesian coordinates in the reference frame of Fig. 6. The fulfillment of the patch test then requires that numerically computed displacements and potentials of any interior node inside the patch follow exactly (up to machine precision) the analytical solution (36). The numerical solution either by poly-CM or poly-SCM is provided by the final matrix system (19) for piezoelectric problems, with $\tilde{\mathbf{f}} = \mathbf{0}$ under Dirichlet BCs only. By partitioning the solution vector \mathbf{x} in (19) into interior \mathbf{x}_i and boundary \mathbf{x}_b unknowns, (19) becomes:

$$\begin{pmatrix} \mathbf{K}^{ii} & \mathbf{K}^{ib} \\ \mathbf{K}^{bi} & \mathbf{K}^{bb} \end{pmatrix} \begin{pmatrix} \mathbf{x}_i \\ \mathbf{x}_b \end{pmatrix} = \begin{pmatrix} \mathbf{0} \\ \mathbf{0} \end{pmatrix}, \quad (37)$$

so that the residual $\|\mathbf{K}^{ii} \mathbf{x}_i - \mathbf{K}^{ib} \mathbf{x}_b\|$ for the numerical solution is zero. The analytical solution $\bar{\mathbf{x}} = (\bar{\mathbf{x}}_i, \bar{\mathbf{x}}_b)^T$, given by (36), does not fulfill exactly (37) and discrepancy from numerical solution is evaluated as:

$$e = \frac{\|\mathbf{K}^{ii} \bar{\mathbf{x}}_i - \mathbf{K}^{ib} \bar{\mathbf{x}}_b\|}{\|\mathbf{K}^{ib} \bar{\mathbf{x}}_b\|}, \quad (38)$$

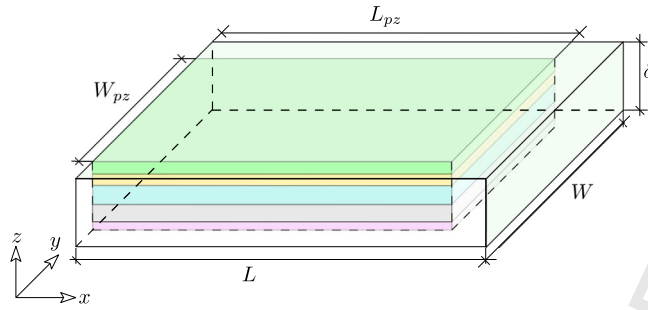


Fig. 7. PPA1001 unimorph cantilever model (polyimide – purple, steel – gray, piezo – cyan, copper – orange, polyester – green; 5-ply structure embedded into polyimide).

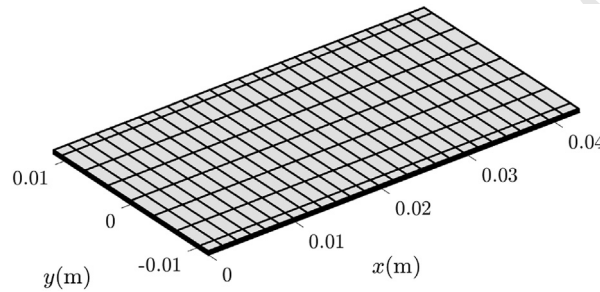


Fig. 8. Hexahedral mesh of PPA1001 unimorph cantilever.

where $\|\cdot\|$ is the vector 2-norm. For the test case considered, discretized by the polyhedral mesh shown in Fig. 6, the discrepancy is $2.2846 \cdot 10^{-14}$, for standard CM, and $2.6716 \cdot 10^{-14}$, for poly-SCM.

6.2. Unimorph piezoelectric cantilever

1) Base PPA 1001 harvester model A realistic 3-D model geometry of a unimorph piezoelectric cantilever (PPA 1001 product type in [44]), which can be used as an actuator (imposing an external voltage) or energy harvester (converting mechanical vibrations into electrical energy) is considered for validating poly-CM. Fig. 7 shows the base model used in simulations. The harvester structure is multi-layered and is made up of five different and perfectly bonded materials (starting from the bottom layer: polyimide, steel, PZT-5H, copper, and polyester). The substrate layer is simulated as a linearly elastic material with isotropic property. Conversely, the piezoelectric substrate (PZT-5H) is modeled as a transverse isotropic linear elastic material with polarization axis directed along the z -axis. The cantilever is clamped at one end (vertical plane $x = 0$). The multi-layered structure with PZT layer (W_{pz} width, L_{pz} length) is embedded into a polyimide structure (δ thickness, W width, L length larger than W_{pz} , L_{pz}). The whole model, which is a Manhattan structure, can be discretized by a structured mesh made of regular hexahedra (Fig. 8).

2) Harvester with dynamic vibration absorber Fig. 9 shows a PPA1001 harvester equipped with a dynamic vibration absorber, which is a small vibrating system tuned to the natural frequency of the harvester [45]. Dynamic vibration absorber is able to modify the frequency response of the harvester and in particular to lower the first natural frequency, which is useful in many applications [3]. In the case here investigated the structural layer of the harvester (steel substrate) is properly extended and shaped in order to create the dynamic vibration absorber. The steel part exceeding the multi-layer structure is described by the following geometric parameters: curvature radius R , center (x_c, y_c) , and length L_a . Curved boundary cannot be discretized by a standard hexahedral mesh (e.g., made with bricks) and a polyhedral mesh is thus required instead (Fig. 10). For the proposed cantilever, model discretization can be easily built from a structured mesh by the carving technique of Section 5.1 and implemented in the numerical code.

Material properties of piezo-layer and substrates are given respectively in Table B.2 and B.3 (Appendix B). Geometric parameters for test model 1 and 2 are given respectively in Table B.4 and B.5 (Appendix B).

Static analysis Numerical codes implementing poly-CM and poly-SCM formulations and solving system (19) for static analyses have been developed. Both harvester models are validated by means of quadratic FEM in static conditions. An external potential $\Phi_{ext} = 10$ V is applied at the upper surface of PZT layer, whereas the lower surface is at the mass potential. Therefore, a beam deflection due to piezoelectric effect is generated, which is assessed by computing the displacement along the beam longitudinal x -axis (coordinates $y = 0$, $z = \delta_{pi} + \delta_{st}$). Reference FEM models used for comparisons are refined till convergence. FEM model for the base PPA1001 harvester is meshed by a structured mesh (7,068 quadratic hexahedra,

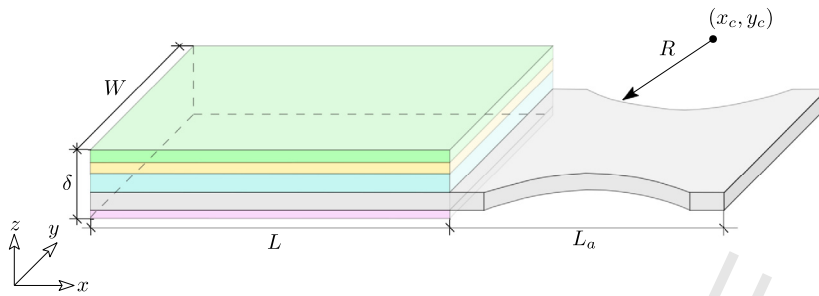


Fig. 9. PPA1001 unimorph cantilever with absorber model (the absorber is the beam extending the structural steel layer of the 5-ply structure).

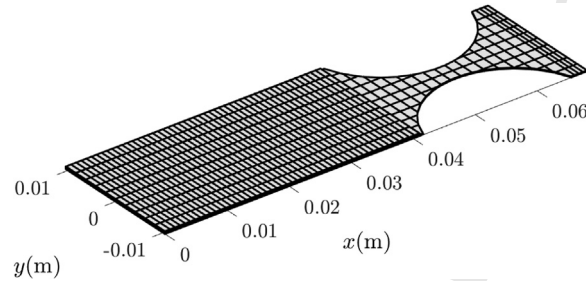


Fig. 10. Polyhedral mesh of PPA1001 unimorph cantilever with absorber.

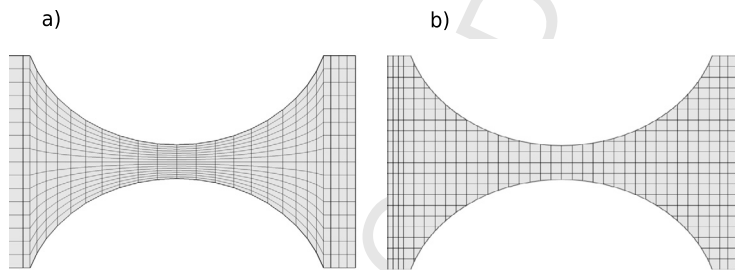


Fig. 11. FEM structured (a) and CM polyhedral (b) meshes of the absorber.

198,370 DoFs) with subdivisions along axis $N_x = 31$, $N_y = 12$ (one subdivision for discretizing the polyimide boundaries) and $N_z = 19$ (five subdivisions for steel and PZT layers and three subdivisions for the other layers). For the harvester with absorber model, a structured mesh is used only for discretizing the multi-layer structure whereas the absorber part is discretized by non-regular hexahedra, with particular care in preparing CAD geometry (the same number of subdivisions has to be used in y direction in order to generate mesh). Fig. 11 shows the structured and polyhedral meshes used by FEM and CM numerical codes. For the harvester with absorber model, the mesh consists in 11,120 quadratic hexahedra (312,110 DoFs) with $N_x = 41$ (11 subdivisions for absorber), $N_y = 16$, and N_z as above.

Fig. 12 shows that z -axis displacement component w calculated from numerical model implementing standard piecewise uniform bases is not accurate due to shear locking. In fact, poly-CM does not attain convergence values (quadratic FEM solution) by increasing the number of DoFs. On the contrary, Fig. 13 shows that face-smoothed formulation provides accurate results even with a model with coarse mesh refinement (14,768 DoFs). Similar results are obtained for test case 2), with polyhedral mesh for poly-CM. In such a case, with almost a half of quadratic FEM DoFs a comparable displacement profile is obtained (Fig. 15), whereas poly-CM does not converge (Fig. 14). Computing performances of both poly-CM and poly-SCM (implemented under Matlab® software environment and simulated on Intel CORE i7-6920HQ CPU@2.9GHz, 16.38 GB RAM) are provided in Table 1. This table shows the overhead involved by the smoothing approach with respect to non-smoothed CM, for each given number of DoFs. Numerical routines for matrix assembly are written in a non-optimized scripting code, based on the use of cycles and cell array data structures. The solution of the final algebraic system is provided by the standard Matlab® backslash operator. The reference FEM model for test case 1 is simulated on the same machine by a commercial FEM software, highly-optimized for numerical computing, in ~ 30 s CPU time (28 s of which are required by direct solver for linear system solution).

Frequency analysis The validation of poly-SCM numerical code is then extended to frequency analysis in which matrix system (20) is solved by sweeping the angular frequency ω in order to identify the characteristic resonances of the harvester.

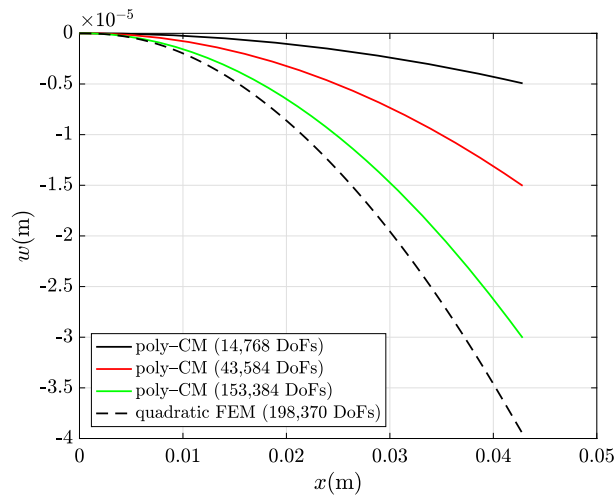


Fig. 12. Displacement along the z-axis computed by poly-CM for an increasing number of DoFs (test case 1). Quadratic FEM (dashed line) taken as a reference.

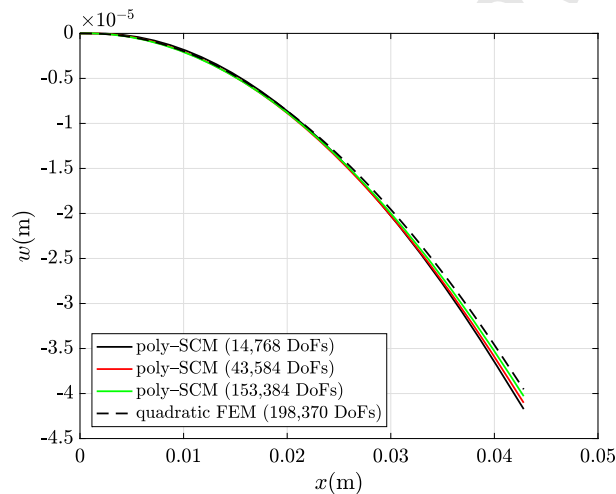


Fig. 13. Displacement along the z-axis computed by poly-SCM for an increasing number of DoFs (test case 1). Quadratic FEM (dashed line) taken as a reference.

Table 1
Computing performances of poly-CM and poly-SCM.

| DoFs | Assembly CPU time (s) | | Solution CPU time (s) | |
|---------|-----------------------|----------|-----------------------|----------|
| | poly-CM | poly-SCM | poly-CM | poly-SCM |
| 14,768 | 14.16 | 110.65 | 1.23 | 2.36 |
| 43,584 | 70.33 | 346.11 | 6.32 | 14.80 |
| 153,384 | 621.03 | 1,359.68 | 75.62 | 270.05 |

Comparisons are made with numerical results (quadratic FEM) and experimental data (only in the case of base cantilever model of PPA 1001 piezo-harvester). The frequency response of the PPA 1001 cantilever is measured by an impulsive testing method (equipment, test rig and methodology are described in detail in [46,47]). The piezo-harvester is connected to an external electrical circuit and different load resistances are considered ($R_{ext} = 12.7 \text{ k}\Omega, 50 \text{ k}\Omega, 1 \text{ M}\Omega$). Frequency response function (FRF) between generated voltage and base acceleration shows a peak of 17 mV/g at 125 Hz (natural frequency f_0) for the base PPA1001 harvester. Hysteretic damping ratio (estimated experimentally by half power method [48]) is $\eta = 0.015$. The initial load resistance is chosen by taking optimal load value, which is determined (according to [49]) as $R_{opt} = (\omega_0 C_{pz})^{-1}$, with $C_{pz} = 0.1 \text{ }\mu\text{F}$ measured harvester capacitance and $\omega_0 = 2\pi f_0$ resonance angular frequency.

Generated voltage at circuit terminals is computed (by both quadratic FEM and poly-SCM) and measured in the frequency range from 120 up to 130 Hz, around the resonance peak. The same mesh used for the static model is used by FEM (with

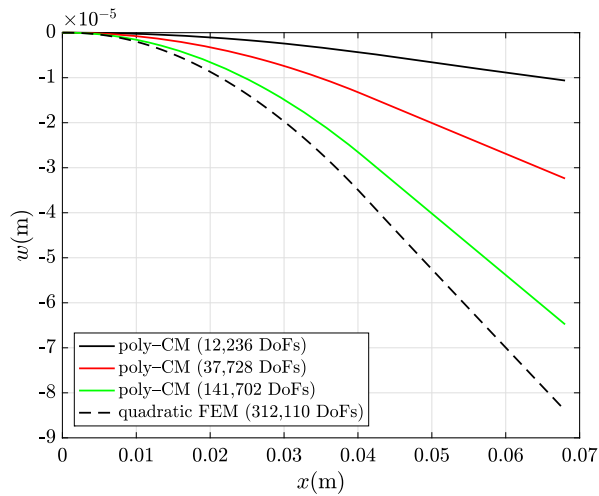


Fig. 14. Displacement along the z-axis computed by poly-CM for an increasing number of DoFs (test case 2). Quadratic FEM (dashed line) taken as a reference.

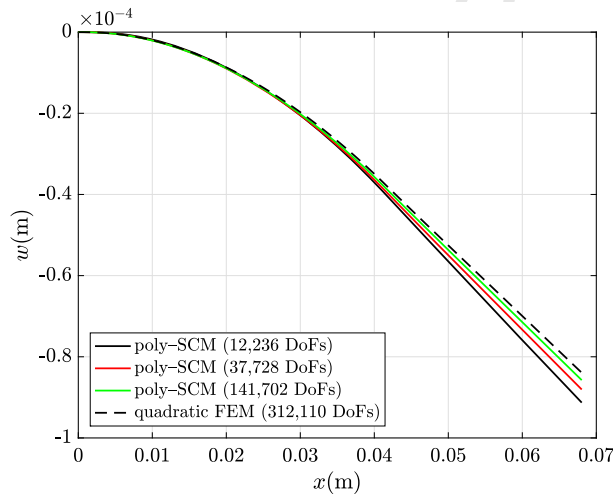


Fig. 15. Displacement along the z-axis computed by poly-SCM for an increasing number of DoFs (test case 2). Quadratic FEM (dashed line) taken as a reference.

198,368 DoFs), whereas for poly-SCM a structured mesh with subdivisions $N_x = 210$, $N_y = 12$, $N_z = 22$ (172,646 DoFs) is used. Figs. 16 and 17 show that FRF modulus and phase are in very good agreement with quadratic FEM results, even though a much lower number of DoFs is needed with poly-SCM. Both numerical models are in good agreement with measurements.

For the test case 2, optimal load resistance is estimated to be $R_{ext} = 22 \text{ k}\Omega$, since resonance frequency is 73 Hz (first mode). It can be observed that main effect of the dynamic vibration absorber is a frequency splitting (i.e. two resonance peaks are generated: the former at lower frequency than the resonance frequency of PPA 1001 alone, the latter at higher frequency), as shown in Figs. 18 and 19. Frequency responses computed by both poly-SCM and quadratic FEM show to be in very good agreement. It should be noted also in this case that convergence is attained by poly-SCM by using a much lower number of DoFs than quadratic FEM (115,008 vs. 181,990) which shows the advantage of using low-order basis functions for multiphysics coupled simulations. Moreover, mesh in correspondence of the absorber part is much less refined (i.e. polymesh does not require a constant number of subdivisions such as structured FEM mesh).

Transient analysis Results of transient smoothed CM model, given by the solution of (21) with the Newmark time-stepping scheme, are compared to both quadratic FEM results and experimental measurements. In experimental tests piezo-harvester is excited by force pulses of different duration. Input base acceleration and output voltage time profiles are measured at

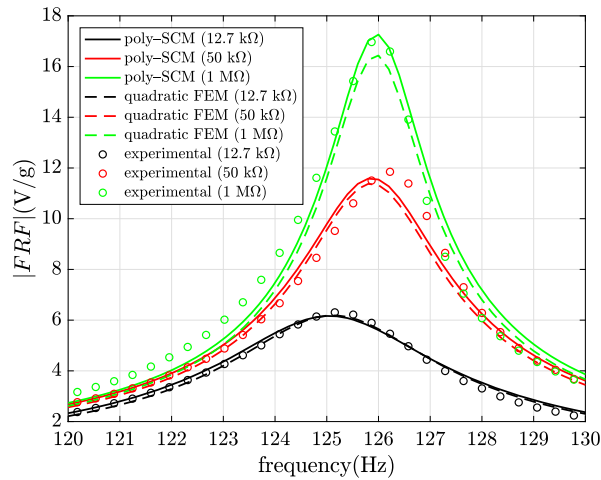


Fig. 16. Frequency response (modulus) of piezo-harvester voltage (PPA1001) for different load resistances. Experimental data (circles) and quadratic FEM (dashed line) taken as a reference.

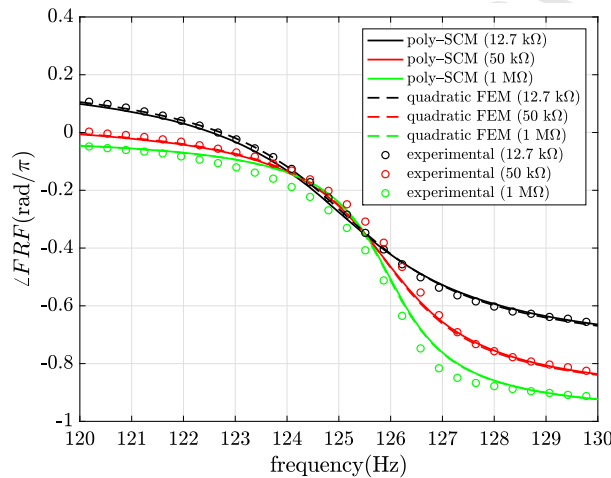


Fig. 17. Frequency response (phase) of piezo-harvester voltage (PPA1001) for different load resistances. Experimental data (circles) and quadratic FEM (dashed line) taken as a reference.

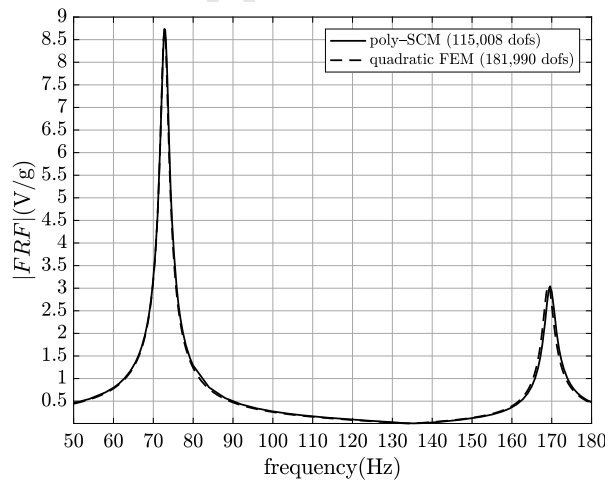


Fig. 18. Frequency response (modulus) of piezo-harvester voltage (PPA1001 with absorber) at the optimal load resistance (22 kΩ). Quadratic FEM (dashed line) taken as a reference.

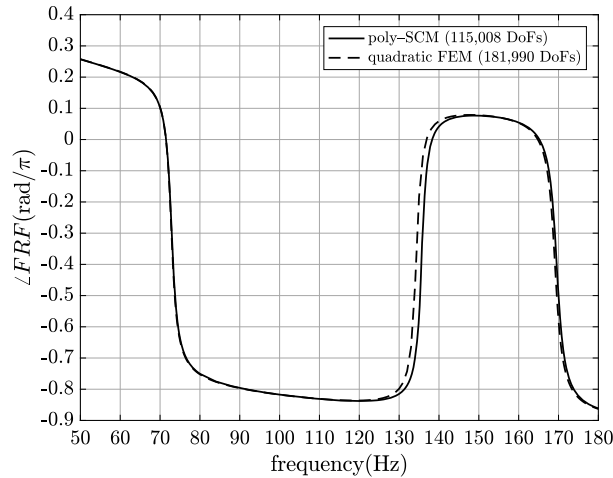


Fig. 19. Frequency response (phase) of piezo-harvester voltage (PPA1001 with absorber) at the optimal load resistance (22 kΩ). Quadratic FEM (dashed line) taken as a reference.

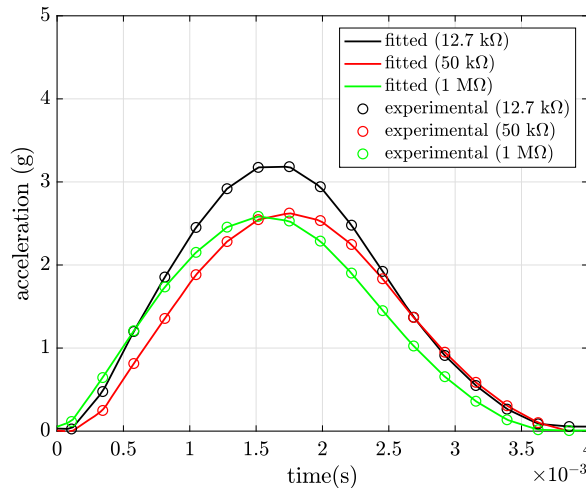


Fig. 20. Interpolated acceleration pulse profiles used for simulating the transient response of piezo-harvester (PPA1001). Experimental data taken as a reference.

the same instants by a data logger. Fig. 20 shows acceleration pulses (4 ms duration) measured and fitted for any test case ($R_{ext} = 12.7 \text{ k}\Omega$, $50 \text{ k}\Omega$, $1 \text{ M}\Omega$). Fitted curves are used as input data for both poly-SCM and FEM models, which provide numerical voltage profiles in a 40 ms time interval. Equivalent Rayleigh's damping model parameters are derived from the hysteretic factor as $\alpha = 0 \text{ s}^{-1}$ and $\beta = \eta/\omega_0 = 19 \mu\text{s}$. The same mesh used for the static and frequency models is used with FEM. Figs. 21–23 show that numerically computed transients are in good agreement with experimental data. In particular, observing first time periods, poly-SCM guarantees a very good accuracy also in the weakly-damped case ($R_{ext} = 1 \text{ M}\Omega$).

7. Conclusion

This work demonstrates that low-order Cell Method schemes used for electromagnetic problems can be adapted to piezoelectric coupled problems. A reformulation of constitutive relationships in terms of displacement gradient makes it possible to split discrete topological and constitutive relationships in the CM framework. Piecewise uniform basis functions for polyhedral grids can be thus used allowing for a general treatment of model discretization. By using the face smoothing technique developed for FEM (which is limited to tetrahedral and hexahedral meshes) novel functions have been proposed. In such a way, locking phenomena arising when low-order basis functions are used for analyzing thin structures can be overcome. A novel numerical procedure (exploiting the carving technique of structured meshes) has been proposed in order to generate polyhedral grids of thin multilayer structures. This mesh construction requires much less effort in CAD model

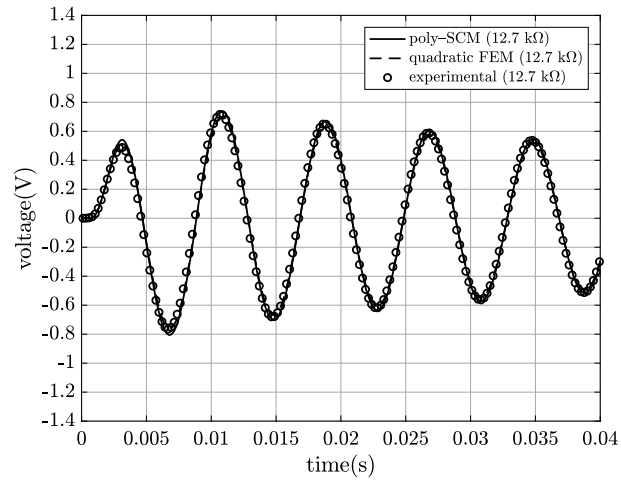


Fig. 21. Voltage transient response of piezo-harvester voltage (PPA1001) with 12.7 k Ω resistance load. Poly-SCM solution compared with quadratic FEM (dashed line) and experimental data (circles).

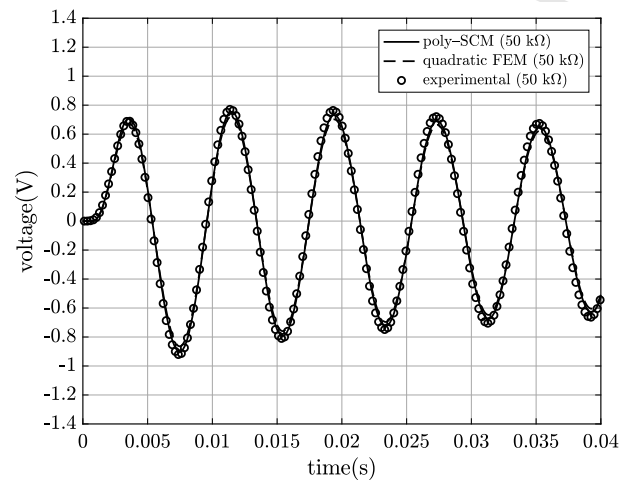


Fig. 22. Voltage transient response of piezo-harvester voltage (PPA1001) with 50 k Ω resistance. Poly-SCM solution compared with quadratic FEM (dashed line) and experimental data (circles).

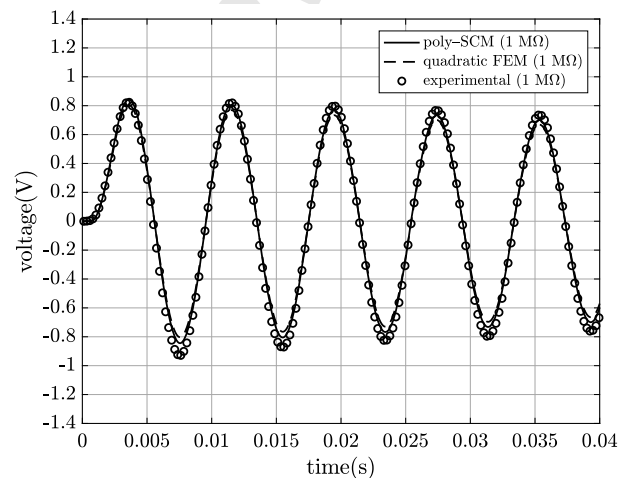


Fig. 23. Voltage transient response of piezo-harvester voltage (PPA1001) with 1 M Ω resistance. Poly-SCM solution compared with quadratic FEM (dashed line) and experimental data (circles).

preparation compared to FEM. Moreover, constitutive matrix assembly is completely Jacobian-free and does not require Gaussian integration, with benefits in terms of code complexity and readability. Test cases show that CM numerical codes for static, frequency, and transient analyses are accurate and reliable even when 3-D models of real-life piezoelectric cantilevers, with complex multilayer structure, are analyzed. The number of DoFs in test cases considered is even smaller than quadratic FEM, with similar accuracy of results. These features show the advantage of adopting low-order elements when 3-D coupled analyses on complex structures need to be carried out.

Acknowledgements

This work was supported by the Università degli Studi di Padova under the grant CPDA142798 (project PRAT14 “Piezoelectric Micro-Electro-Mechanical Power Supply for Automotive Wireless Sensors”). The authors would like also to thank Dr. Sundararajan Natarajan of the Department of Mechanical Engineering, Indian Institute of Technology, Madras (India), for providing the polyhedral mesh used in the patch test.

Appendix A

1 Polygonal mesh clipping algorithm.

```

1:  $P \leftarrow \text{length}(\text{poly})$ 
2: for  $k = 1 : P$  do
3:    $\text{polygon} \leftarrow \text{poly}[k]$ 
4:    $\text{vert} \leftarrow \text{polygon} \cap \text{circle}$ 
5:   if  $\text{length}(\text{vert}) = 2$  then
6:      $\text{nod2d} \leftarrow \text{vert}$ 
7:      $\text{edge} \leftarrow \text{vert}(1) \cup \text{vert}(2)$ 
8:      $\{\text{curve}[1], \text{curve}[2]\} \leftarrow \text{polygon} \setminus \text{edge}$ 
9:      $\text{poly}[P + 1] \leftarrow (\text{vert}(1), \text{vert}(2)) \cup \text{curve}[1]$ 
10:     $\text{poly}[P + 2] \leftarrow (\text{vert}(2), \text{vert}(1)) \cup \text{curve}[2]$ 
11:   end if
12: end for

```

2 Polygonal mesh sweeping algorithm.

```

1: for  $k = 1 : N_2$  do
2:    $n \leftarrow (k - 1)N_{2d} + 1 : kN_{2d}$  ▷ add vertexes for  $k$ -th layer
3:    $\text{nod3d}(n, \cdot) \leftarrow (\text{nod2d}, \text{vecz}(k))$ 
4:    $e \leftarrow (k - 1)E_{2d} + 1 : kE_{2d}$  ▷ add horizontal edges
5:    $\mathbf{G}_{3d}(e, n) \leftarrow \mathbf{G}_{2d}$ 
6:    $f \leftarrow (k - 1)F_{2d} + 1 : kF_{2d}$  ▷ add horizontal faces
7:    $\mathbf{C}_{3d}(f, e) \leftarrow \mathbf{C}_{2d}$ 
8: end for
9:  $e_{\max} \leftarrow \max e, f_{\max} \leftarrow \max f$ 
10: for  $k = 1 : N_2 - 1$  do
11:    $n \leftarrow (k - 1)N_{2d} + 1 : kN_{2d}$  ▷ add vertical edges
12:    $\mathbf{G}_{3d}(e + e_{\max}, n) \leftarrow -\mathbb{I}_{N_{2d}}$ 
13:    $\mathbf{G}_{3d}(e + e_{\max}, n + N_{2d}) \leftarrow +\mathbb{I}_{N_{2d}}$ 
14:    $e \leftarrow (k - 1)E_{2d} + 1 : kE_{2d}$  ▷ add vertical faces
15:    $\mathbf{C}_{3d}(e + f_{\max}, e) \leftarrow +\mathbb{I}_{E_{2d}}$ 
16:    $\mathbf{C}_{3d}(e + f_{\max}, e + E_{2d}) \leftarrow -\mathbb{I}_{E_{2d}}$ 
17:    $\mathbf{C}_{3d}(e + f_{\max}, n + E_{2d}) \leftarrow \mathbf{G}_{2d}$ 
18:    $f \leftarrow (k - 1)F_{2d} + 1 : kF_{2d}$  ▷ add polyhedral cells
19:    $\mathbf{D}_{3d}(f, f) \leftarrow -\mathbb{I}_{F_{2d}}$ 
20:    $\mathbf{D}_{3d}(f, f + F_{2d}) \leftarrow \mathbb{I}_{F_{2d}}$ 
21:    $\mathbf{D}_{3d}(f, e + F_{2d}) \leftarrow \mathbf{C}_{2d}$ 
22: end for
23: for  $e = 1 : E_{3d}$  do
24:    $\text{edgs}[e] \leftarrow \{\text{find}(\mathbf{G}_{3d}(e, \cdot) = -1), \text{find}(\mathbf{G}_{3d}(e, \cdot) = 1)\}$ 
25: end for
26: for  $f = 1 : F_{3d}$  do
27:    $\text{facs}[f] \leftarrow \text{find}(\mathbf{C}_{3d}(f, \cdot))$ 
28: end for
29: for  $v = 1 : V_{3d}$  do
30:    $\text{cells}[v] \leftarrow \text{find}(\mathbf{D}_{3d}(v, \cdot))$ 
31: end for

```


3 Constitutive matrix assembly for standard CM.

```

1: for  $v = 1 : V_{3d}$  do
2:   cell  $\leftarrow$  cells[v]
3:   for  $f = 1 : \text{length}(\text{cell})$  do
4:     face  $\leftarrow$  cell[f]
5:     edges  $\leftarrow$  edges  $\cup$  eds[face]
6:   end for
7:   c(0)  $\leftarrow$  centre(cell)
8:   for  $e = 1 : E_V$  do
9:     edge  $\leftarrow$  edges[e]
10:    {face(1), face(2)}  $\leftarrow$  edgtofac[e]
11:    c(1 : 2)  $\leftarrow$  centre(face(1 : 2))
12:    c(3)  $\leftarrow$  centre(edge)
13:     $\mathbf{e}[e] \leftarrow$  nod3d(edge[2],  $\cdot$ ) - nod3d(edge[1],  $\cdot$ )
14:     $\tilde{\mathbf{f}}_e[e] \leftarrow \frac{1}{2}(\mathbf{c}(0) - \mathbf{c}(3)) \times (\mathbf{c}(1) - \mathbf{c}(2))$ 
15:    supp[e]  $\leftarrow \frac{1}{3} \mathbf{e} \cdot \tilde{\mathbf{f}}_e$ 
16:   end for
17:   for  $i, j = 1 : 4$  do
18:     for  $h, k = 1 : 3$  do
19:       mloc(h, k)  $\leftarrow$  m(map(i, j, h, k))
20:     end for
21:     for  $e, e' = 1 : E_V$  do
22:        $\mathbf{w}_e \leftarrow$  basis( $\mathbf{e}, \tilde{\mathbf{f}}_e, \text{vol}(\text{cell})$ )
23:        $\mathbf{w}_{e'} \leftarrow$  basis( $\mathbf{e}', \tilde{\mathbf{f}}_{e'}, \text{vol}(\text{cell})$ )
24:        $\mathbf{w}_{e'} \leftarrow \mathbf{w}_{e'} \cdot \text{mloc}$ 
25:        $ie \leftarrow 4(\text{iedgs}[e] - 1) + i$ 
26:        $ie' \leftarrow 4(\text{iedgs}[e'] - 1) + j$ 
27:       mat(ie, ie')  $\leftarrow$  mat(ie, ie') +  $\sum_k \text{supp}[k] \mathbf{w}_e(k, \cdot) \cdot \mathbf{w}_{e'}(k, \cdot)$ 
28:     end for
29:   end for
30: end for

```

\triangleright basis change due to material property

4 Constitutive matrix assembly for smoothed CM.

```

1: for  $f = 1 : F_{3d}$  do
2:   smoothface  $\leftarrow$  facs[f]
3:   adjcells  $\leftarrow$  facetocells[f]
4:   for  $v = 1 : \text{length}(\text{adjcells})$  do
5:     cell  $\leftarrow$  adjcells[v]
6:     edges, c, e,  $\tilde{\mathbf{f}}_e$ , supp  $\leftarrow$  ...
7:     for  $e = 1 : E_V$  do
8:       if edges  $\cap$  eds[smoothface]  $\neq \emptyset$  then
9:         edge  $\leftarrow$  edges[e]
10:        c(5)  $\leftarrow$  centre(smoothface)
11:        v(1 : 2)  $\leftarrow$  nod3d(edge(1 : 2),  $\cdot$ )
12:        svol[v][e]  $\leftarrow \frac{1}{6}(\mathbf{c}(0) - \mathbf{v}(1)) \cdot [\mathbf{e} \times (\mathbf{c}(5) - \mathbf{v}(1))]$ 
13:      end if
14:    end for
15:     $\mathbf{w}_e[v] \leftarrow$  basis( $\mathbf{e}, \tilde{\mathbf{f}}_e, \text{vol}(\text{cell})$ )
16:     $\hat{\mathbf{w}}_e[v] \leftarrow (\text{svol}[v][1] / \sum_k \text{svol}[v][k]) \mathbf{w}_e[v]$ 
17:  end for
18:   $\hat{\mathbf{w}}_e[v] \leftarrow (\sum_k \text{svol}[v][k] / \sum_{v,k} \text{svol}[v][k]) \mathbf{w}_e[v]$ 
19:  for  $i, j = 1 : 4$  do
20:    for  $v, v' = 1 : \text{length}(\text{adjcells})$  do
21:      for  $e, e' = 1 : E_V, E_{V'}$  do
22:         $\hat{\mathbf{w}}_{e'} \leftarrow \hat{\mathbf{w}}_{e'} \cdot \text{mloc}$ 
23:         $ie \leftarrow 4(\text{iedgs}[e] - 1) + i$ 
24:         $ie' \leftarrow 4(\text{iedgs}[e'] - 1) + j$ 
25:        mat(ie, ie')  $\leftarrow$  mat(ie, ie') +  $\sum_{v,k} \text{svol}[v][k] \hat{\mathbf{w}}_e[v] \cdot \hat{\mathbf{w}}_{e'}[v']$ 
26:      end for
27:    end for
28:  end for
29: end for

```

\triangleright compute variables as Algorithm 3
 \triangleright compute smoothing region volume

\triangleright smoothing face centroid

\triangleright smoothing on $\hat{v}_f \cap v$

\triangleright smoothing on \hat{v}_f

\triangleright mloc computed as Algorithm 3

Appendix B

Table 2

PZT-5H material properties.

| Elastic stiffness matrix c_E (Pa) | Piezoelectric matrix e (C/m ²) | Dielectric matrix ϵ_s |
|-------------------------------------|--|---|
| $C_{11} = 1.272 \cdot 10^{11}$ | $e_{31} = -6.62281$ | $\epsilon_{11} = 1704.4 \cdot \epsilon_0$ |
| $C_{12} = 8.021 \cdot 10^{10}$ | $e_{32} = e_{31}$ | $\epsilon_{22} = 1704.4 \cdot \epsilon_0$ |
| $C_{13} = 8.467 \cdot 10^{10}$ | $e_{33} = 23.2403$ | $\epsilon_{11} = 1433.6 \cdot \epsilon_0$ |
| $C_{22} = C_{11}$ | $e_{15} = 17.0345$ | |
| $C_{23} = C_{13}$ | | |
| $C_{33} = 1.174 \cdot 10^{11}$ | | |
| $C_{44} = 2.299 \cdot 10^{10}$ | | |
| $C_{55} = C_{44}$ | | |
| $C_{66} = 2.347 \cdot 10^{10}$ | | |

 $(\epsilon_0 = 8.85 \cdot 10^{-12}$ F/m is the vacuum electric permittivity)**Table 3**

Substrate material properties.

| Material | Elastic modulus (GPa) | Poisson's ratio (·) | Density (kg/m ³) |
|------------------|-----------------------|---------------------|------------------------------|
| Polyester | 3.65 | 0.48 | 1380 |
| Copper | 110 | 0.34 | 1300 |
| Steel (AISI 304) | 193 | 0.29 | 8000 |
| Polyimide | 4.1 | 0.34 | 1410 |
| PZT-5H | – | – | 7800 |

Table 4

Geometric parameters of PPA-1001 unimorph cantilever (base model).

| Parameter | Symbol | Value (mm) |
|----------------------|---------------|------------|
| Substrate width | W_{pz} | 20.8 |
| Cantilever width | W | 23.3 |
| Substrate length | L_{pz} | 41.0 |
| Cantilever length | L | 42.83 |
| Polyimide thickness | δ_{pi} | 0.03 |
| Steel thickness | δ_{st} | 0.15 |
| PZT thickness | δ_{pz} | 0.15 |
| Copper thickness | δ_{cp} | 0.03 |
| Polyester thickness | δ_{pe} | 0.05 |
| Cantilever thickness | δ | 0.41 |

Table 5

Geometric parameters of unimorph cantilever with integrated absorber.

| Parameter | Symbol | Value (mm) |
|--|---------------|---------------|
| Cantilever width | W | 20.8 |
| Cantilever length | L | 41.0 |
| Polyimide thickness | δ_{pi} | 0.03 |
| Steel thickness | δ_{st} | 0.15 |
| PZT thickness | δ_{pz} | 0.15 |
| Copper thickness | δ_{cp} | 0.03 |
| Polyester thickness | δ_{pe} | 0.05 |
| Cantilever thickness | δ | 0.41 |
| Absorber length | L_a | 27 |
| Absorber curvature radius | R | $L_a/2$ |
| Absorber curvature centre (x coordinate) | x_c | $L + L_a/2$ |
| Absorber curvature centre (y coordinate) | y_c | $W/2 + 0.3 R$ |

Appendix C. Supplementary material

Supplementary material related to this article can be found online at <https://doi.org/10.1016/j.jcp.2019.02.012>.

References

- [1] G.A. Rincón-Mora, S. Yang, Tiny piezoelectric harvesters: principles, constraints, and power conversion, *IEEE Trans. Circuits Syst. I, Regul. Pap.* 63 (2016) 639–649.
- [2] S. Priya, D.J. Inman, *Energy Harvesting Technologies*, Springer, 2009.
- [3] T.J. Kázmierski, S. Beeby, *Energy Harvesting Systems: Principles, Modelling, and Applications*, Springer, 2011.
- [4] M. Kaltenbacher, *Numerical Simulation of Mechatronic Sensors and Actuators*, Springer, 2015.
- [5] J.E. Bishop, A displacement-based finite element formulation for general polyhedra using harmonic shape functions, *Int. J. Numer. Methods Eng.* 97 (2014) 1–31.
- [6] P. Milbradt, T. Pick, Polytope finite elements, *Int. J. Numer. Methods Eng.* 73 (2008) 1811–1835.
- [7] M. Wicke, M. Botsch, M. Gross, A finite element method on convex polyhedra, *Comput. Graph. Forum* 26 (2007) 355–364.
- [8] A.L. Gain, T. Cameron, G.H. Paulino, On the virtual element method for three-dimensional linear elasticity problems on arbitrary polyhedral meshes, *Comput. Methods Appl. Mech. Eng.* 282 (2014) 132–160.
- [9] L.B. da Veiga, C. Lovadina, D. Mora, A virtual element method for elastic and inelastic problems on polytope meshes, *Comput. Methods Appl. Mech. Eng.* 295 (2015) 327–346.
- [10] H. Chi, L.B. da Veiga, G.H. Paulino, Some basic formulations of the Virtual Element Method (VEM) for finite deformations, *Comput. Methods Appl. Mech. Eng.* 318 (2017) 148–192.
- [11] E. Tonti, Why starting from differential equations for computational physics? *J. Comput. Phys.* 257 (2014) 1260–1290.
- [12] F. Moro, L. Codecasa, A 3-D hybrid cell method for induction heating problems, *IEEE Trans. Magn.* 53 (2017) 1–4.
- [13] E. Tonti, F. Zarantonello, Algebraic formulation of elastostatics: the Cell Method, *Comput. Model. Eng. Sci.* 39 (2009) 201–236.
- [14] E. Tonti, F. Zarantonello, Algebraic formulation of elastodynamics: the Cell Method, *Comput. Model. Eng. Sci.* 64 (2010) 37–70.
- [15] P. Bettini, E. Brusa, M. Munteanu, R. Specogna, F. Trevisan, Static behavior prediction of microelectrostatic actuators by discrete geometric approaches, *IEEE Trans. Magn.* 44 (2008) 1606–1609.
- [16] F. Moro, P. Alotto, F. Freschi, M. Guarnieri, A cell method formulation of 3-D electrothermomechanical contact problems with mortar discretization, *IEEE Trans. Magn.* 48 (2012) 503–506.
- [17] P. Alotto, F. Freschi, M. Repetto, C. Rosso, *The Cell Method for Electrical Engineering and Multiphysics Problems: An Introduction*, Lecture Notes in Electrical Engineering, vol. 230, Springer, 2013.
- [18] A. Bossavit, Discrete magneto-elasticity: a geometrical approach, *IEEE Trans. Magn.* 46 (2010) 3485–3491.
- [19] L. Codecasa, R. Specogna, F. Trevisan, Base functions and discrete constitutive relations for staggered polyhedral grids, *Comput. Methods Appl. Mech. Eng.* 198 (2009) 1117–1123.
- [20] T.J.R. Hughes, *The Finite Element Method: Linear Static and Dynamic Finite Element Analysis*, Dover Publications, Inc., 2000.
- [21] G.R. Liu, N.T. Trung, *Smoothed Finite Element Methods*, CRC Press, 2010.
- [22] W. Zeng, G.R. Liu, Smoothed finite element methods (S-FEM): an overview and recent developments, *Arch. Comput. Methods Eng.* 25 (2018) 397–435.
- [23] D. Sohn, J. Han, Y. Cho, S. Im, A finite element scheme with the aid of a new carving technique combined with smoothed integration, *Comput. Methods Appl. Mech. Eng.* 254 (2013) 42–60.
- [24] C. Lee, H. Kim, J. Mim, S. Im, Polyhedral elements using an edge-based smoothed finite element methods for nonlinear elastic deformations of compressible and nearly incompressible materials, *Comput. Mech.* 60 (2017).
- [25] D. Sohn, S. Jin, Polyhedral elements with strain smoothing for coupling hexahedral meshes at arbitrary nonmatching interfaces, *Comput. Methods Appl. Mech. Eng.* 293 (2015) 92–113.
- [26] A. Francis, A. Ortiz-Bernardin, S. Bordas, N. Sundararajan, Linear smoothed polygonal and polyhedral finite elements, *Int. J. Numer. Methods Eng.* 109 (2017) 1263–1288.
- [27] Z. He, G. Li, Z. Zhong, A. Cheng, G. Zhang, E. Li, G. Liu, An ES-FEM for accurate analysis of 3D mid-frequency acoustics using tetrahedron mesh, *Comput. Struct.* 106–107 (2012) 125–134.
- [28] E. Li, Z. He, X. Xu, An edge-based smoothed tetrahedron finite element method (ES-T-FEM) for thermomechanical problems, *Int. J. Heat Mass Transf.* 66 (2013) 723–732.
- [29] E. Li, Z. He, J. Hu, X. Long, Volumetric locking issue with uncertainty in the design of locally resonant acoustic metamaterials, *Comput. Methods Appl. Mech. Eng.* 324 (2017) 128–148.
- [30] H. Nguyen-Xuan, G.R. Liu, T. Nguyen-Thoi, C. Nguyen-Tran, An edge-based smoothed finite element method for analysis of two-dimensional piezoelectric structures, *Smart Mater. Struct.* 18 (2009) 065015.
- [31] L. Chen, Y.W. Zhang, G.R. Liu, H. Nguyen-Xuan, Z.Q. Zhang, A stabilized finite element method for certified solution with bounds in static and frequency analyses of piezoelectric structures, *Comput. Methods Appl. Mech. Eng.* 241–244 (2012) 65–81.
- [32] G. Gafforelli, *Piezoelectric Vibration Micro Energy Harvesters*, Ph.D. thesis, Doctoral School in Structural, Seismic and Geotechnical Engineering (XXVII cycle), Politecnico di Milano, 2015.
- [33] IEEE, *IEEE Standard on Piezoelectricity*, ANSI/IEEE 176-1987 1, 1988, pp. 1–74.
- [34] L. Codecasa, Refoundation of the cell method using augmented dual grids, *IEEE Trans. Magn.* 50 (2014) 497–500.
- [35] Z. He, E. Li, G. Liu, G. Li, A. Cheng, A mass-redistributed finite element method (MR-FEM) for acoustic problems using triangular mesh, *J. Comput. Phys.* 323 (2016) 149–170.
- [36] D.J. Ewins, *Modal Testing: Theory, Practice and Application*, 2nd ed., Research Studies Press, Philadelphia, PA, 2000.
- [37] Y. Kagawa, T. Tsuchiya, T. Kataoka, T. Yamabuchi, T. Furukawa, Finite element simulation of dynamic responses of piezoelectric actuators, *J. Sound Vib.* 191 (1996) 519–538.
- [38] J.S. Chen, C.T. Wu, S. Yoon, Y. You, A stabilized conforming nodal integration for Galerkin mesh-free methods, *Int. J. Numer. Methods Eng.* 50 (2001) 435–466.
- [39] G.R. Liu, K.Y. Dai, T.T. Nguyen, A smoothed finite element method for mechanics problems, *Comput. Mech.* 39 (2007) 859–877.
- [40] T. Nguyen-Thoi, G.R. Liu, K.Y. Lam, G.Y. Zhang, A face-based smoothed finite element method (FS-FEM) for 3-D linear and geometrically non-linear solid mechanics problems using 4-node tetrahedral elements, *Int. J. Numer. Methods Eng.* 78 (2009) 324–353.
- [41] E. Li, J. Chen, Z. Zang, J. Fang, G.R. Liu, Q. Li, Smoothed finite element method for analysis of multi-layered systems-applications in biomaterials, *Comput. Struct.* 168 (2016) 16–29.
- [42] G. Liu, A generalized gradient smoothing technique and the smoothed bilinear form for Galerkin formulation of a wide class of computational methods, *Int. J. Comput. Methods* 05 (2008) 199–236.
- [43] Z.J. Wang, Improved formulation for geometric properties of arbitrary polyhedra, *AIAA J.* 37 (1999) 1326–1327.
- [44] Midé, PPA PRODUCTS: Datasheet & User Manual, <https://www.mouser.com/ds/2/606/ppa-piezo-product-datasheet-844547.pdf>, 2018 (Accessed 20 June 2018), online.
- [45] A. Doria, C. Medé, G. Fanti, D. Desideri, A. Maschio, F. Moro, Development of piezoelectric harvesters with integrated trimming devices, *Appl. Sci.* 8 (2018) 557.

- 1 [46] A. Doria, C. Medé, D. Desideri, A. Maschio, L. Codecasa, F. Moro, Improvement of harvesters for tires by means of multi-physics simulation, in: Proc. of 1
2 the ASME Design Engineering Technical Conference, vol. 3, 2017, pp. 1–10. 2
- 3 [47] A. Doria, C. Medé, D. Desideri, A. Maschio, L. Codecasa, F. Moro, On the performance of piezoelectric harvesters loaded by finite width impulses, Mech. 3
4 Syst. Signal Process. 100 (2018) 28–42. 4
- 5 [48] C.W. de Silva, Vibration Fundamental and Practice, second edition, Taylor Francis, Boca Raton, FL, 2007. 5
- 6 [49] J. Dicken, P.D. Mitcheson, I. Stoianov, E.M. Yeatman, Power-extraction circuits for piezoelectric energy harvesters in miniature and low-power applica- 6
7 tions, IEEE Trans. Power Electron. 27 (2012) 4514–4529. 7
- 8 8
9 9
10 10
11 11
12 12
13 13
14 14
15 15
16 16
17 17
18 18
19 19
20 20
21 21
22 22
23 23
24 24
25 25
26 26
27 27
28 28
29 29
30 30
31 31
32 32
33 33
34 34
35 35
36 36
37 37
38 38
39 39
40 40
41 41
42 42
43 43
44 44
45 45
46 46
47 47
48 48
49 49
50 50
51 51
52 52
53 53
54 54
55 55
56 56
57 57
58 58
59 59
60 60
61 61

UNCORRECTED PROOF

1 XMLVIEW: extended

2 Appendix C. Supplementary material

3 The following is the Supplementary material related to this article.

4 Label: MATLAB file


5 Caption: This is a MATLAB file of Fig. ?,

6 Link: APPLICATION : mmc1

7
8
9
10
11
12
13
14
15
16
17
18
19
20
21
22
23
24
25
26
27
28
29
30
31
32
33
34
35
36
37
38
39
40
41
42
43
44
45
46
47
48
49
50
51
52
53
54
55
56
57
58
59
60
61

Sponsor names

Do not correct this page. Please mark corrections to sponsor names and grant numbers in the main text.

407  Università degli Studi di Padova, country=Italy, grants=CPDA142798

UNCORRECTED PROOF

Highlights

- Novel low-order discretization scheme on polyhedral meshes.
- Cell Method extended to 3-D piezo-elastic problems.
- Cell Method extended to smoothing technique for avoiding shear locking.
- Matrix assembly completely Jacobian-free and Gaussian integration not required.
- Accuracy of Smoothed Cell Method similar to second-order FEM with a much lower number of degrees of freedom.